The Midlatitude Resolution Capability of Sea Level Fields Constructed from Single and Multiple Satellite Altimeter Datasets

DIANA J. M. GREENSLADE, DUDLEY B. CHELTON, AND MICHAEL G. SCHLAX

College of Oceanic and Atmospheric Sciences, Oregon State University, Corvallis, Oregon

ABSTRACT

A formalism recently developed for determining the effects of sampling errors on objectively smoothed fields constructed from an irregularly sampled dataset is applied to investigate the relative merits of single and multiple satellite altimeter missions. For small smoothing parameters, the expected squared error of smoothed fields of sea surface height (SSH) varies geographically at any particular time and temporally at any particular location. The philosophy proposed here for determining the resolution capability of SSH fields constructed from altimeter data is to identify smoothing parameters that are sufficiently large to satisfy two criteria: 1) the expected squared errors of the estimates of smoothed SSH over the space–time estimation grid must be either spatially and temporally homogeneous to within some a priori specified degree of tolerance or smaller than some a priori specified threshold, and 2) the space–time estimation grid on which smoothed SSH estimates are constructed must satisfy the Nyquist criteria for the wavenumbers and frequencies included in the smoothed fields.

The method is illustrated here by adopting a specified tolerance of 10% variability and a nominal expected squared error threshold of 1 cm^2 to determine the resolution capabilities of SSH fields constructed from 10 single and multiple combinations of altimeter measurements by TOPEX/Poseidon, the ERS Earth Resource Satellites, and Geosat. Because of the lack of coordination of the orbit configurations of these satellites (different repeat periods and different orbit inclinations), the mapping resolution capabilities of the combined datasets are not significantly better than those of fields constructed from TOPEX/Poseidon data alone. The benefits of coordinated multiple missions are demonstrated by consideration of several multiple combinations of 10-, 17-, and 35-day orbit configurations.

1. Introduction

A primary objective of many ongoing altimetric studies of sea surface height (SSH) variability is to investigate the role of the oceans in global climate variability on seasonal and longer timescales. Although the resolution capability of altimeter observations along the satellite ground track is of order 10 km and 10 days, the large lateral spacing of neighboring ground tracks and the time intervals between samples near a given location severely limit the space scales and timescales that can be resolved in three-dimensional SSH fields constructed from altimeter data. The full potential of such applications of altimeter data cannot be realized until the effects of the unique sampling characteristics of the observations on the accuracies of the estimated SSH fields are fully understood. The objective of this study is to develop a formalism for rational and objective guidance in choosing the degree of spatial and temporal smoothing that should be applied when constructing SSH fields from altimeter data.

Ultimately, the highest resolution SSH fields will undoubtedly be obtained by assimilating altimeter data into ocean circulation models as recently discussed, for example, by Verron et al. (1996). At the present time, however, we feel that there is considerable merit in constructing SSH fields solely from altimeter data in order to provide completely independent assessment of the accuracies of presently available ocean circulation models. The present study therefore considers SSH fields constructed without the use of a dynamical model to effectively interpolate between the altimeter observations.

The mapping resolution problem is perhaps best illustrated by examples in which SSH fields are constructed from simulated altimeter data with an arbitrarily prescribed, but quite plausible, degree of smoothing. Simulated altimeter datasets were obtained by subsampling the output of an eddy-admitting global ocean circulation model along satellite ground tracks. The model used here is run 11 of the primitive equation, multilayer model, with realistic coastlines and bathymetry, developed by the Parallel Ocean Program (POP) at Los Alamos National Laboratory (Dukowicz and Smith 1994). The model grid for run 11 consists of a Mercator grid with 0.28° longitudinal spacing and $(0.28°) \cos\theta$ latitude spacing, where θ is latitude.

Corresponding author address: Dr. Dudley B. Chelton, College of Oceanic and Atmospheric Sciences, Oregon State University, Oceanography Administration Building 104, Corvallis, OR 97331-5503.

The technical details and quantitative accuracy of this model are of secondary importance for present purposes. It should be noted, however, that it is well established that the present generation of this model and other ocean general circulation models of this class significantly underestimates the mesoscale variability that is the major source of sampling errors in smoothed SSH maps constructed from altimeter data (e.g., Treguier 1992; Wilkin and Morrow 1994; Stammer et al. 1996; McClean et al. 1996). The errors deduced here from simulated altimeter data are therefore a lower bound for the sampling errors that can be expected from actual altimeter data.

A snapshot of smoothed SSH in a region of the central North Pacific obtained by interpolating the complete gridded model output onto a 0.25° grid with spatial and temporal smoothing that retains scales longer than 2.5° and 30 days is shown in Fig. 1a. The smoothed SSH field constructed from simulated 10-day repeat TOPEX/Poseidon (referred to hereafter as TP) data by subsampling the model along the satellite ground tracks and smoothing onto the 0.25° interpolation grid with the same 2.5° by 30 day smoothing is shown in Fig. 1b. Although the large-scale features of the "true" smoothed field in Fig. 1a are reproduced in the TP map, there are significant discrepancies in many of the finer details. This is easily seen from the map of the differences in Fig. 2a. Bands of errors parallel to some of the satellite ground tracks are clearly evident, as are bull's-eyes of locally large errors in excess of 3 cm. The precise locations of the bull's-eyes depend on the temporal distribution of samples along the nearby ground tracks. Generally, the largest errors occur near the centers of the diamond-shaped regions formed by the intersections of ascending and descending ground tracks. These errors are manifested as sampling artifacts such as the apparent eddy near 32.5°N, 178°W in Fig. 1b. Because of the large lateral spacing of the ground tracks, the TP sampling pattern is clearly incapable of resolving spatial scales as short as 2.5°.

The spatial sampling problem inherent in the TP ground track pattern is greatly reduced by the much smaller lateral spacing of the ground tracks of the 35-day repeat European *ERS-1* and *ERS-2* Earth Resource Satellites. In this case, however, the long repeat period is the most limiting factor. The smoothed SSH field constructed from simulated ERS data is shown in Fig. 1c, and the corresponding error map is shown in Fig. 2b. The dense spatial coverage of the ERS ground tracks eliminates bull's-eyes of locally large errors. However, the long orbit repeat period results in bands of estimation errors that are much larger than those apparent in the SSH map constructed from simulated TP data. These bands of large errors are centered along the satellite ground tracks that are sampled near the beginning or end of the temporal span of ERS data used to construct the 30-day smoothed SSH field. The 30-day averages are therefore poorly constrained in these regions of the map. A particularly extreme example is the band of greater than 3-cm errors that corresponds to the ridge
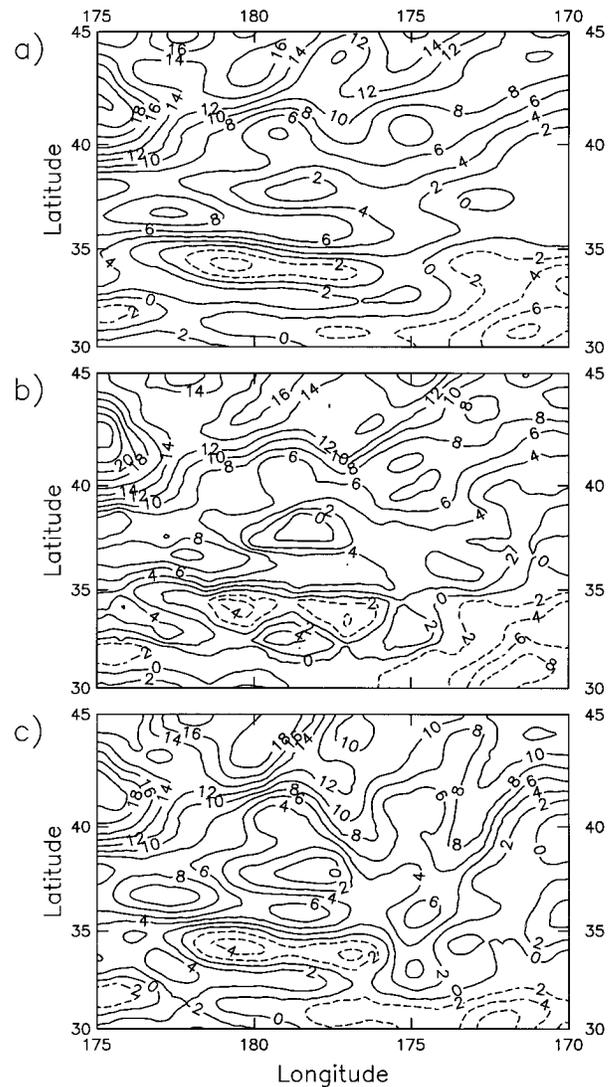

FIG. 1. Example maps of smoothed SSH constructed from the output of an eddy-admitting global ocean circulation model by smoothing (a) the complete gridded model output, (b) simulated TOPEX/Poseidon (TP) data, and (c) simulated ERS data. The simulated altimeter data were obtained by interpolating the model output to the altimeter measurement times and locations along the satellite ground tracks. The smoothing in all cases was designed to retain scales longer than 2.5° and 30 days, Contour interval is 2 cm.

of erroneously high SSH in Fig. 1c extending south-southwest from the northeast corner of the domain. The ERS sampling pattern clearly cannot resolve signals with temporal scales as short as 30 days.

Because of the complementary good temporal sampling of TP and good spatial sampling of ERS, it may seem intuitive that the two altimeter datasets could be combined to resolve the 2.5° by 30-day scales considered here. As shown in Fig. 2c, however, this is not the case. Although the magnitudes of the errors are somewhat smaller on average, there are still many areas where the errors are larger than 2 cm and some areas
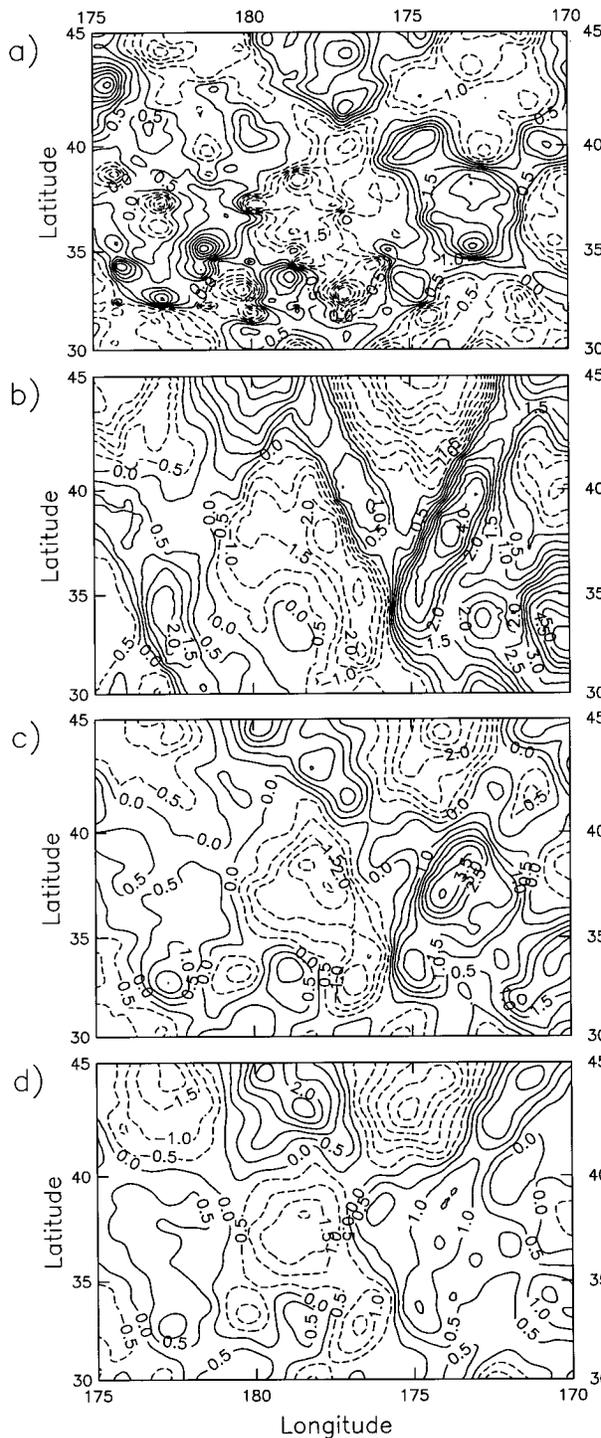
FIG. 2. The differences between the smoothed SSH estimates in Fig. 1a obtained from the complete gridded model output and smoothed SSH estimates constructed from (a) the simulated TP estimate shown in Fig. 1b, (b) the simulated ERS estimate shown in Fig. 1c, (c) a simulated tandem TP and ERS mission, and (d) a simulated triplet TP, ERS, and GFO mission. In all cases, the smoothing retained scales longer than 2.5° and 30 days. Contour interval is 0.5 cm.
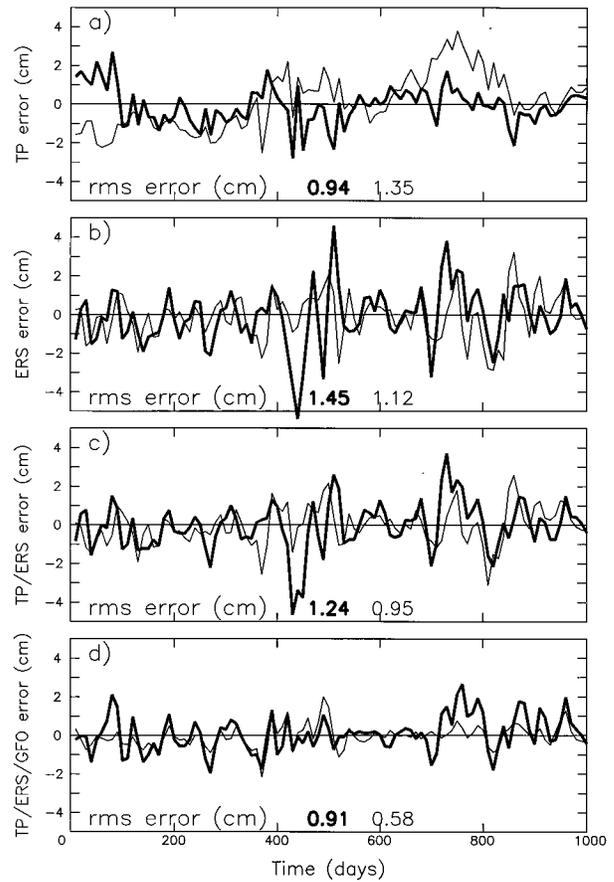

FIG. 3. Time series of the differences between smoothed SSH at two locations constructed from the complete gridded model output and from (a) simulated TP data, (b) simulated ERS data, (c) simulated combined TP and ERS data, and (d) simulated combined TP, ERS, and GFO data. The smoothing applied in all cases retains scales longer than 2.5° by 30 days. Heavy and thin lines correspond to locations 37.1°N, 174.3°W and 34.8°N, 178.6°W, respectively. The corresponding rms errors are labeled by the bold and thin numbers.

where the errors are larger than 3 cm. Even when data from simultaneous simulated measurements by TP, ERS, and Geosat follow-on (GFO) are combined, there are areas with errors as large as 2.5 cm (Fig. 2d). Since 2–3-cm errors are comparable to the amplitudes of the SSH signals on these space scales and timescales, we conclude that none of the maps constructed from single, tandem, or triplet combinations of TP, ERS, and GFO data are capable of resolving SSH signals with spatial scales of 2.5° and temporal scales of 30 days.

In addition to varying geographically, the errors in smoothed SSH fields constructed from altimeter data vary temporally at any given location. This is illustrated in Fig. 3, in which time series of errors are shown for 2.5° × 30 day smoothed estimates constructed at two locations from single, tandem, and triplet combinations of simulated TP, ERS, and GFO data.

For the 37°N, 174°W location (heavy lines in Fig. 3), the rms errors are smallest for the estimates obtained

from TP sampling alone and largest from the ERS sampling alone. Of particular significance is the very counterintuitive result that the accuracies of estimates constructed from the TP sampling are actually degraded when combined with ERS sampling and are only slightly improved when combined with both ERS and GFO sampling.

The characteristics of the sampling errors are more intuitive at the 35°N, 178°E location (thin lines in Fig. 3). Here the errors are largest in smoothed SSH estimates constructed from the TP sampling alone and successively smaller for SSH estimates constructed from ERS sampling, tandem TP–ERS sampling, and triplet TP–ERS–GFO sampling.

As the ''measurements'' in these simulated altimeter datasets are error free, the regions of large mapping errors in Fig. 2 arise at locations where sample observations are poorly distributed geographically or temporally for estimating the $2.5° \times 30$ day scales retained by the smoothing applied here to the data. Even if the number of ''nearby'' observations is large, the smoothed SSH cannot be estimated accurately if all or most of the observations are located in one corner of the $2.5°$ area centered on the estimation location or near the beginning or end of the 30-day averaging period centered on the estimation time.

The simulations presented here clearly demonstrate the need for an objective strategy for selecting appropriate smoothing parameters in order to avoid spurious features in SSH fields constructed from altimeter data. A framework and theory for determining the resolution capability of smoothed fields of a scalar variable constructed from an irregularly sampled dataset was developed by Schlax and Chelton (1992, hereafter referred to as SC92). Unlike the simulations above, the method does not rely on an ocean circulation model that simulates mesoscale variability with questionable veracity. Rather, the technique is based on a space–time autocorrelation function of the SSH field that is prescribed on the basis of hydrographic and altimeter observations. The method has been applied to the 17-day repeat sampling pattern of the Geosat and GFO altimeters by Chelton and Schlax (1994, hereafter referred to as CS94), who concluded that this orbit configuration could resolve SSH variations with spatial scales of about 3° in latitude and longitude and temporal scales of about 30 days.

The CS94 study considered sampling errors in smoothed SSH estimates constructed only at the crossovers of ascending and descending ground tracks. In the present study, the methodology of SC92 and CS94 is refined and extended and it is argued that sampling errors must also be considered at the centers of the diamond patterns formed by the intersecting ascending and descending ground tracks. When this is done, it is found that spatial smoothing of 3° is insufficient for the Geosat and GFO sampling pattern according to the criteria proposed here.

The philosophy and an objective set of criteria for determining the resolution capability of SSH fields constructed from altimeter data are discussed in section 2; the technical details of the method are summarized in appendix A. The emphasis here is on applications of the method for midlatitude mapping of SSH (latitudes near 30°). The decreased autocorrelation length scales at higher latitudes are at least partially offset by the improved sampling owing to the convergence of satellite ground tracks at higher latitudes. Similarly, the coarser ground-track spacing at lower latitudes is partially offset by increased autocorrelation length scales. The results presented here are therefore reasonably representative of a broad range of latitudes. This broad geographical representation is further aided by consideration of spatial smoothing in degrees rather than kilometers.

The mapping resolution capabilities for the individual Geosat, ERS, and TP altimeter missions are presented in sections 3, 4, and 5, respectively. The mapping resolution capability of the tandem TP and ERS mission is investigated in section 6 and the triplet TP, ERS, and GFO mission is considered in section 7. In an effort to determine the optimum orbit configuration for the TOPEX/Poseidon follow-on altimeter (recently named Jason), the results for various possible tandem TP and Jason orbit configurations are presented in section 8. A similar analysis for tandem *ERS-1* and *ERS-2* orbit configurations is presented in section 9.

2. The method

The complexity of sampling errors in SSH fields constructed from altimeter data has been discussed previously by Wunsch (1989). Because of the irregular space–time sampling imposed by the satellite orbit constraints, sample estimates of the spectral characteristics of SSH variability at any particular wavenumber and frequency are contaminated by aliasing from other wavenumbers and frequencies that are not resolved by the sampling pattern. Wunsch (1989) presents a formalism in which SSH is represented by a set of discrete harmonics at prescribed wavenumbers and frequencies. Estimates of the expected squared errors of the amplitudes and phases of the specified harmonics can then be obtained by underdetermined least squares.

The method presented by Wunsch (1989) quantifies the relative merits of different orbit configurations for resolving specified wavenumbers and frequencies of interest. For studies of large-scale, low-frequency variability, it was concluded that the TP 10-day sampling pattern yields smaller uncertainties than does the 17-day Geosat sampling pattern, evidently because the longer repeat period of the Geosat orbit results in a greater degree of aliasing of short-period mesoscale variability.

The formalism developed by SC92 and CS94 addresses the problem of irregular sampling from a different, but related, perspective. Rather than considering the expected squared error of specified harmonics, the

total effect of unresolved aliasing over all frequencies and wavenumbers is determined from the expected squared error of the SSH estimate constructed at a specific time and location by a prescribed smoothing algorithm. Such an estimate is recognized as a low-pass-filtered version of the data. Consideration of different filter parameters allows the overall mapping resolution capability of the irregular sampling pattern to be quantified.

a. The criteria for determining mapping resolution capability

The method proposed by SC92 and CS94 is extended here by developing a set of objective criteria for determining the mapping resolution capability of a given sampling pattern. The starting point for the methodology is based on the fact that most algorithms for smoothing irregularly spaced data can be expressed as a linear combination of the observations. As summarized in appendix A, the technique proposed by SC92 to determine the mapping resolution capability of an irregularly sampled dataset was developed for an arbitrarily defined linear objective estimate. It is argued in appendix A that the detailed formalism used to define the linear estimate is of secondary importance. Any specific linear estimate can be characterized by half-power filter cutoff frequency and wavenumbers that are effectively prescribed by the coefficients of the linear estimate.

The particular linear estimate used in this study is the quadratic loess smoother summarized in appendix B. The degree of smoothing is defined by ''smoothing parameters'' d_x, d_y, and d_t that correspond to the spatial and temporal half spans of the data incorporated in the loess estimates. It is shown in CS94 that the low-pass cutoff zonal and meridional wavenumbers k_c and l_c and frequency f_c are related to the loess smoothing parameters by $k_c \approx d_x^{-1}$, $l_c \approx d_y^{-1}$, and $f_c \approx d_t^{-1}$. A distinct advantage of the quadratic loess smoother is thus that the filtering properties of the smoother are explicitly defined in a very simple and convenient manner in terms of the half spans of the smoother. In the applications here, only isotropic smoothing is considered, in which case $d_x = d_y \equiv d_s$.

The technique introduced by SC92 is designed specifically to address the practical problem of the complexity of spatially and temporally inhomogeneous estimation errors that arise when the energetic scales of variability are inadequately sampled, as they are in all altimeter observations of SSH. Ideally, the degree of smoothing required to reduce such inhomogeneities to acceptable levels is dictated by the required accuracy of objectively smoothed fields constructed from irregularly sampled observations. In rare cases, this can be specified a priori. It is more often the case that quantitative statements of the required accuracy are not available. For example, a reasonable goal for the accuracy of smoothed SSH estimates is probably about 1 cm for

studies of large-scale, low-frequency SSH variability. However, it is difficult to state with confidence whether 1 cm is essential or whether the required accuracy could be relaxed to 2 cm, for example. This can be problematic when selecting the smoothing parameters of the objective estimation algorithm; a modest difference in the tolerable uncertainty of the smoothed fields can result in a dramatic difference in the required smoothing parameters.

The method proposed by SC92 and CS94 provides a means of establishing, in the absence of quantitative a priori knowledge of the required accuracy, an estimate of the wavenumbers and frequencies that can be resolved by a specified arbitrary sampling pattern. The basic philosophy is very simple and intuitively appealing: the sampling errors of the smoothed fields should be spatially and temporally homogeneous.

The total expected squared error of an objective estimate can be partitioned into contributions from measurement errors and sampling errors. Wunsch (1989) showed that the total error of estimates constructed from altimeter data is generally dominated by sampling errors and that measurement errors are of secondary importance. The sampling error component is wholly embodied in the expected squared bias (ESB), which is determined for a prescribed form for the linear estimate from knowledge of the estimation and observation locations and the power spectral density of the signal (see appendix A).

It is important to note that actual data values are not required to estimate the ESB. As in CS94, the spectral characteristics of SSH variability that are used for the calculations described in sections 3–9 assume an autocorrelation function that is Gaussian in both space and time, with an isotropic spatial decorrelation scale of 50 km and a temporal decorrelation scale of 30 days. This autocorrelation function was deduced from midlatitude hydrographic data by Shen et al. (1986) and is consistent with midlatitude autocorrelation functions estimated from time series and alongtrack TP altimeter data by Stammer (1997, manuscript submitted to *J. Phys. Oceanogr.*). The TP data suggest somewhat longer spatial scales in the Tropics and shorter spatial scales at high latitudes.

To avoid difficulties arising from incomplete knowledge of the geographical distribution of SSH variance over the ocean, the SSH spectrum is normalized by the signal variance for the present applications. The resulting normalized ESB is referred to as the relative expected squared bias (RESB). A typical rms of SSH variability is about 10 cm, corresponding to a signal variance of 100 cm². For error-free measurements, an RESB of 0.01 thus corresponds typically to an rms estimation error of about 1 cm. An RESB of 0.04 corresponds typically to an rms estimation error of 2 cm.

The approach of the proposed method for determining the mapping resolution capability is to reduce spatial and temporal inhomogeneities of the sampling errors by

increasing the smoothing parameters of the objective estimation algorithm. Although this sacrifices the high resolution possible where the field is densely sampled, it is preferable to undersmoothing the data, in which case short scales are resolvable in densely sampled regions but only long scales are resolvable in coarsely sampled regions. As shown by the simulated examples in the introduction, such inhomogeneities of resolution can easily be misinterpreted as geographical or temporal variability of the wavenumber–frequency spectral characteristics of the SSH field, rather than artifacts of the sampling errors.

In practice, of course, the sampling errors of objectively smoothed fields are never perfectly homogeneous spatially and temporally. We propose a 10% spatial and temporal variation of the RESB as an operational definition of "statistically homogeneous." The alterations of the conclusions regarding mapping resolution capabilities when a more liberal RESB variability criterion of 20% is adopted are discussed in section 10. In the altimeter applications of interest here, the somewhat arbitrary (and perhaps application-specific) 10% RESB variability criterion was found to coincide closely with subjectively determined "diminishing return" values of the smoothing parameters d_x, d_y, and d_t. Increasing the smoothing parameters beyond the values required to satisfy the 10% RESB variability criterion generally yielded only marginal decreases of the inhomogeneity of the sampling errors. However, the spatial and temporal inhomogeneities typically increased rapidly for smaller values of the smoothing parameters.

It is shown in appendix A that a particular choice of smoothing parameters defines the filtering properties of the linear objective smoother used to construct smoothed SSH estimates (see also SC92 and CS94). An essential second criterion that must be considered in order to determine the mapping resolution capability of an irregularly sampled dataset is therefore that the interpolation grid on which smoothed estimates are constructed must satisfy the Nyquist sampling theorem for the wavenumbers passed by the smoother. Otherwise, the gridded SSH fields alias the short-scale variability that is not resolved by the grid. Since the low-pass filter cutoff wavenumbers and frequency are $k_c \approx d_x^{-1}$, $l_c \approx d_y^{-1}$, and $f_c \approx d_t^{-1}$ for the quadratic loess smoother considered here, the spatial and temporal grid spacings Δx, Δy, and Δt must be smaller than $d_x/2$, $d_y/2$, and $d_t/2$, respectively. Equivalently, the minimum spatial and temporal smoothing parameters must be at least twice as large as the grid spacing of the interpolation grid. The importance of this criterion is illustrated in section 3.

Although any arbitrary rectangular interpolation grid could be adopted, there is merit in choosing a grid that is geometrically connected to the ground-track pattern. The diamond patterns formed by the intersections of the ascending and descending ground tracks of an altimeter orbit are shown in Fig. 4a. The dimensions of the longitudinal separation $\Delta\phi$ of neighboring crossover points
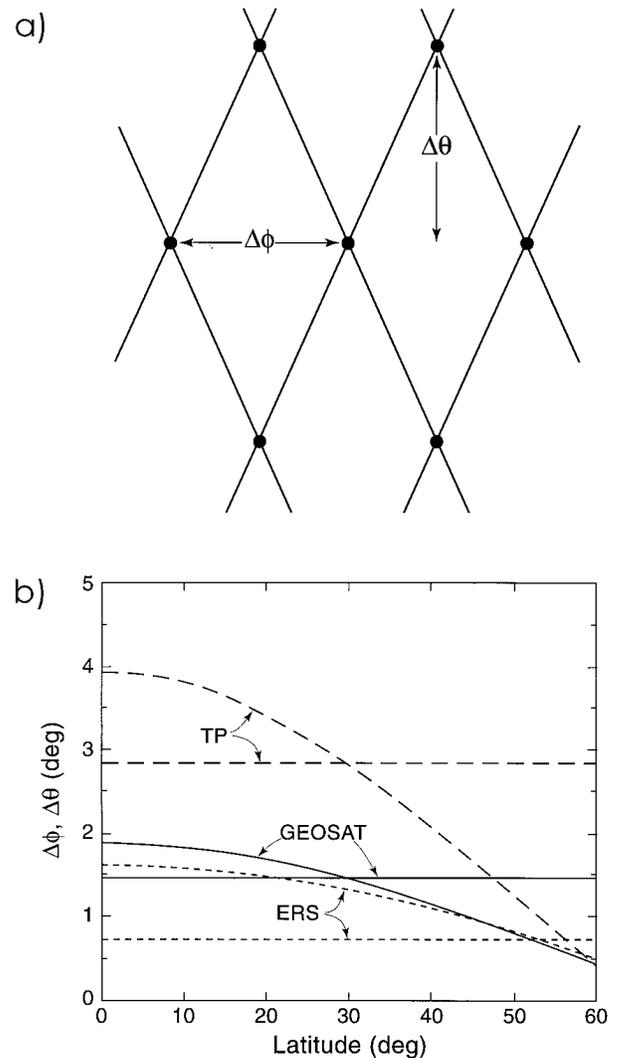

FIG. 4. (a) A schematic ground-track pattern mapped out by the ascending and descending ground tracks of an exact-repeat altimetric satellite. The longitudinal and latitudinal separations of neighboring crossover points are labeled as $\Delta\phi$ and $\Delta\theta$, respectively. (b) The latitudinal variation of $\Delta\phi$ (constant with latitude) and $\Delta\theta$ (decreasing with increasing latitude) of neighboring crossover points for TP (long-dashed curves), Geosat (solid curves), and ERS (short-dashed curves).

along a given latitude of crossovers and the latitudinal separation $\Delta\theta$ of neighboring latitudes of crossovers are shown as a function of latitude in Fig. 4b. Since the number of individual ground tracks in a single orbit repeat period is obviously the same at all latitudes sampled by the altimeter, $\Delta\phi$ in degrees of longitude is independent of latitude. However, $\Delta\theta$ decreases toward the turning latitudes of the orbit. The decrease of $\Delta\theta$ with increasing latitude is especially rapid with TP because of its low 66° orbit inclination. At the midlatitude locations near 30° that are of primary interest here, it can be seen from Fig. 4b that $\Delta\theta \approx \Delta\phi \approx 2.8°$ for TP,

$\Delta\theta \approx \Delta\phi \approx 1.5°$ for Geosat, and $\Delta\theta \approx 2\Delta\phi \approx 1.4°$ for ERS.

In this study, we consider rectangular interpolation grids consisting of diamond centers and crossovers. From Fig. 4a, it can be seen that the resulting longitudinal grid spacing is $\Delta x = 0.5\Delta\phi$ and the latitudinal grid spacing is $\Delta y = \Delta\theta$. The advantage of such an interpolation grid is that the spatial distribution of observations about any crossover is the same as that near any other crossover, likewise for diamond centers. For sufficiently large d_t, the RESB over the entire interpolation grid can therefore be characterized by considering the RESB time series at only two locations (one of the crossovers and one of the diamond centers). An arbitrary rectangular grid would require examination of the RESB time series at each individual interpolation location in order to establish the mapping resolution capability of the dataset for that particular grid.

b. Additional considerations

There are two important points that should be considered with regard to the 10% RESB variability criterion proposed in section 2a. The first is that with multidimensional datasets, there is no single combination of the multiple smoothing parameters that yields 10% variability of the RESB. Resolution in one dimension can be improved by increasing the smoothing in either or both of the other dimensions, while still satisfying the 10% RESB variability criterion. The best trade-off of smoothing in the various dimensions will depend on the specific application. For the altimetric studies of SSH variability on seasonal and longer timescales that are of interest here, quadratic loess temporal smoothing parameters as large as $d_t \sim 50$ days are acceptable. The corresponding low-pass cutoff frequency of $f_c = d_t^{-1}$ is comparable to that obtained with the monthly means traditionally used to investigate low-frequency variability of the ocean. (The cutoff frequency of an N-day block average is $f_c \approx 0.6/N$.) We thus define the "best" mapping resolution capability of a particular altimeter orbit configuration to be the highest spatial resolution that satisfies the 10% RESB variability criterion when $d_t \leq 50$ days.

The second point to be considered is that the 10% RESB variability criterion can clearly be relaxed if the magnitudes of the RESB values are sufficiently small. As noted previously, however, quantitative statements of what constitutes "sufficiently small" are often difficult to formulate. If such a criterion can be established a priori, then there may be little need for the formalism proposed here; the user can simply increase the smoothing parameters until the RESB values at all estimation times and locations are smaller than the desired threshold value.

For smoothed fields of SSH variability, 1 cm is perhaps a reasonable specification of threshold rms variability below which the 10% RESB variability criterion

can be relaxed. As noted in section 2a, this corresponds typically to an RESB of 0.01. While errors of 1 cm may be tolerable in regions where the signal amplitudes are about 10 cm, such errors are likely too large in regions where signal amplitudes are only a few centimeters. For this reason, specification of a threshold criterion as a fraction of the signal variance (i.e., the RESB) is probably more appropriate than specification of a threshold criterion in units of centimeters. The alteration of the conclusions regarding mapping resolution capabilities when a more liberal threshold mean RESB of 0.04 is adopted are discussed in section 10.

The procedure followed in sections 3–9 to determine the mapping resolution capability of the altimeter orbit configurations is to compute time series of the RESB at a crossover and a diamond center at daily intervals over the satellite repeat period for a wide range of combinations of spatial and temporal smoothing parameters. As described in appendix A, the RESB is completely determined from knowledge of the estimation and observation times and locations and the spectral properties of the SSH field; actual data values are not required to obtain the RESB. The mapping resolution capability is deduced from contour plots of (a) the mean of the RESB time series averaged over the two locations and (b) the maximum deviation of the two RESB time series from the mean RESB, expressed as a percentage of the mean RESB. The contour of 0.01 threshold mean RESB and the contour of 10% RESB variability (shown by a heavy line in each contour plot of RESB variability) are the diagnostic tools used to define the mapping resolution capability of the sampling pattern. In the altimetric applications considered here, it was never possible to relax the 10% RESB variability criterion since the magnitudes of the RESB values were always larger than a threshold RESB value of 0.01 for smoothing parameters that achieved the 10% variability criterion.

3. The mapping resolution capability of Geosat

The exact repeat period of the Geosat altimeter is 17.0505 days (hereafter referred to as 17 days), with a data record that extends from 8 November 1986 to 31 December 1989. The U.S. Navy is expected to launch a Geosat follow-on altimeter satellite in 1997 that will sample the same 17-day ground track as the Geosat exact-repeat mission. Using the spatially and temporally homogeneous RESB criterion discussed in section 2a, CS94 have previously argued that the minimum spatial and temporal scales of SSH variability that can be resolved by the Geosat and GFO ground-track pattern are 3° by 30 days. This conclusion was based on the RESB of smoothed SSH estimates constructed only at ground-track crossover points. It was presumed that a constant RESB at the arbitrarily specified estimation locations was a sufficient criterion for determining the mapping resolution capability of the sampling pattern.

The CS94 analysis overlooks the Nyquist sampling

criterion summarized in section 2a. For the Geosat sampling pattern, a smoothing parameter of $d_s = 3°$ requires a rectangular interpolation grid spacing of $\Delta x = \Delta y \leq 1.5°$. The longitudinal separation of Geosat crossover locations is about 1.5° along each latitude of crossovers. At midlatitudes, the latitudinal separation of crossovers is also about 1.5° (see Fig. 4b), but the crossovers along neighboring crossover latitudes are shifted longitudinally by 0.75°. An estimation grid at just the crossovers therefore consists of a staggered 1.5° grid, rather than the rectangular 1.5° grid required to satisfy the Nyquist sampling theorem.

As discussed in section 2a, rectangular interpolation grids consisting of ground track crossovers and diamond centers are used throughout this study. For Geosat, the midlatitude spacing of this interpolation grid is $\Delta x = 0.75°$ and $\Delta y \approx 1.5°$. For this grid, an isotropic smoothing parameter of $d_s = 3°$ considered by CS94 is double the grid resolution required to satisfy the Nyquist criterion in the zonal direction and is just adequate to satisfy the Nyquist criterion in the meridional direction at midlatitudes.

Time series of RESB computed as described in appendix A for estimates constructed at 1-day intervals with smoothing parameters $(d_s, d_t) = (3°, 30 \text{ days})$ at Geosat diamond centers and crossover locations satisfy the 10% RESB variability criterion at each location individually. However, the RESB at each location differs by about 30% from the mean value averaged over the two locations. This choice of smoothing parameters therefore does not satisfy the 10% RESB spatial variability criterion. Contrary to CS94, we thus conclude that SSH fields constructed from Geosat data are not able to resolve scales as short as 3° with a temporal smoothing parameter of $d_t = 30$ days. This conclusion is supported visually by the "freckled" appearance of global SSH maps constructed from Geosat data with these smoothing parameters.

The temporal mean and the corresponding maximum deviation (expressed as a percentage of the mean) of the RESB time series over all times at a Geosat crossover location and a diamond center are contoured in Fig. 5a. All of the combinations shown have $d_s \geq 3°$ and therefore also satisfy the Nyquist criterion. It can be seen that the highest possible spatial resolution that satisfies the 10% RESB variability criterion is about 4.25°, which is achieved when the temporal smoothing is $d_t \gtrsim 35$ days. In the context of more traditional block averages, the combination $(d_s, d_t) = (4.25°, 35 \text{ days})$ is comparable to approximately 2.5° × 21 day block averages.

It is apparent from Fig. 5a that the temporal resolution can be improved to as short as 25 days by increasing the spatial smoothing to $d_s = 6°$. This higher temporal resolution is unnecessary for the studies of SSH variability on seasonal and longer timescales that are of interest here. Moreover, the 6° spatial smoothing eliminates variability on shorter scales that may be of interest

in such studies. We therefore conclude that 4.5° × 35 days is the best mapping resolution capability for present purposes.

4. The mapping resolution capability of ERS

The 35-day repeat phases of the ERS satellites (13 April 1992–20 December 1993 for Phase C of *ERS-1,* 21 March 1995–31 May 1996 for Phase G of *ERS-1,* and 29 August 1995 through the present for *ERS-2*) is effectively double the repeat period of Geosat. The ground-track pattern is therefore approximately twice as dense as that of Geosat. The dimensions of the interpolation grid of crossovers and diamond centers is $\Delta x \approx 0.35°$, $\Delta y \approx 1.4°$ at midlatitudes (see Fig. 4b).

The ERS ground tracks over a portion of the North Atlantic are shown in Fig. 6. Although the orbit inclinations differ, the temporal sampling of the ERS ground track pattern for the first 17.5 days of the 35-day repeat period (heavy lines in Fig. 6) is qualitatively very similar to that of the Geosat 17-day repeat orbit (see also Fig. 4b and Fig. 7b below). During the second half of the ERS 35-day repeat period, essentially the same ground-track pattern is mapped out again, except it is shifted longitudinally as shown by the thin lines in Fig. 6 so as to interleave the ground tracks sampled during the first half of the repeat period. Thus, in addition to the 3-day subcycle discussed in appendix A, there is a 17.5-day subcycle in the ERS 35-day repeat orbit.

The mean and variability of time series of RESB for smoothed estimates constructed at an ERS diamond center and crossover point are shown in Fig. 5b. Combinations of smoothing parameters that satisfy the 10% RESB variability criterion include approximately (4°, 30 days), (3.25°, 50 days), and (5.5°, 22 days). For a temporal smoothing parameter of $d_t = 35$ days, the spatial mapping resolution capability of the ERS sampling pattern is essentially the same as that obtained from the Geosat sampling pattern. The RESB magnitude for $(d_s, d_t) = (4.25°, 35 \text{ days})$ is somewhat lower for ERS (0.044) than for Geosat (0.052). By increasing the temporal smoothing to $d_t = 50$ days (the maximum allowable value of d_t suggested in section 2b to define the best mapping resolution capability for the altimeter applications of interest here), the spatial resolution of SSH fields can be reduced to about 3.25° for the ERS sampling pattern but remains 4.25° for the Geosat sampling pattern. By analogy with traditional block averages, a resolution of 3.25° × 50 days is comparable to a block average of 2° × 30 days.

5. The mapping resolution capability of TOPEX/ Poseidon

The repeat period of the TP altimeter is 9.9156 days (hereafter referred to as 10 days), with a data record that extends from 2 October 1992 through the present. This relatively short repeat period results in ground

a) GEOSAT   Mean RESB   % RESB variability

b) ERS   Mean RESB   % RESB variability

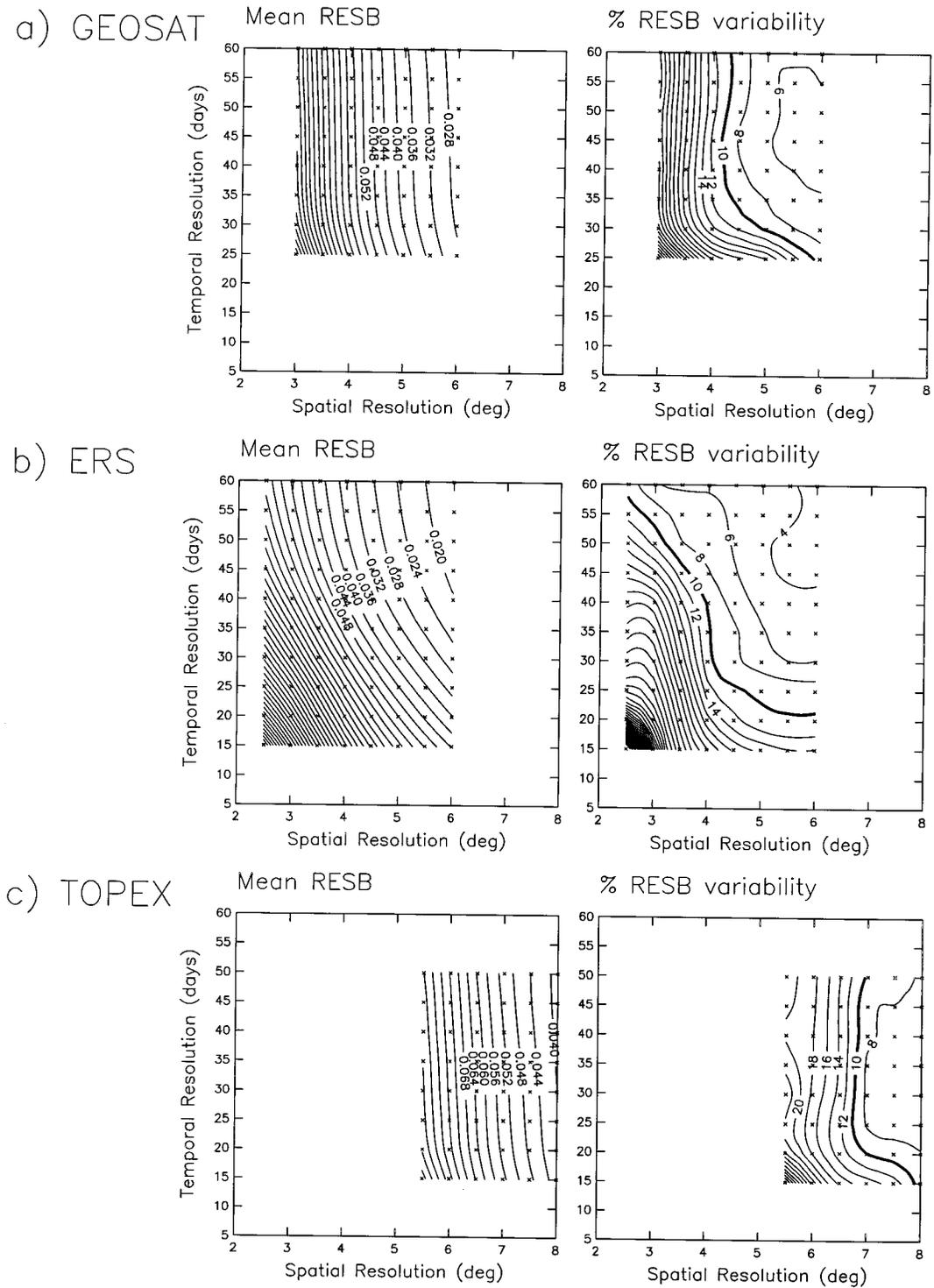c) TOPEX   Mean RESB   % RESB variability

FIG. 5. The mean RESB (left panels) and the RESB variability (right panels) over the orbit repeat periods for smoothed estimates constructed at a diamond center and a crossover at 1-day intervals for (a) the Geosat 17-day repeat, (b) the ERS 35-day repeat, and (c) the TP 10-day repeat sampling patterns. The RESB variabilities in the right panels correspond to the maximum temporal and spatial deviation of the RESB time series from the mean at the diamond center and crossover, expressed as a percentage of the mean RESB shown in the left panels. Contour intervals are 0.004 for the mean RESB and 2% for the RESB variability.
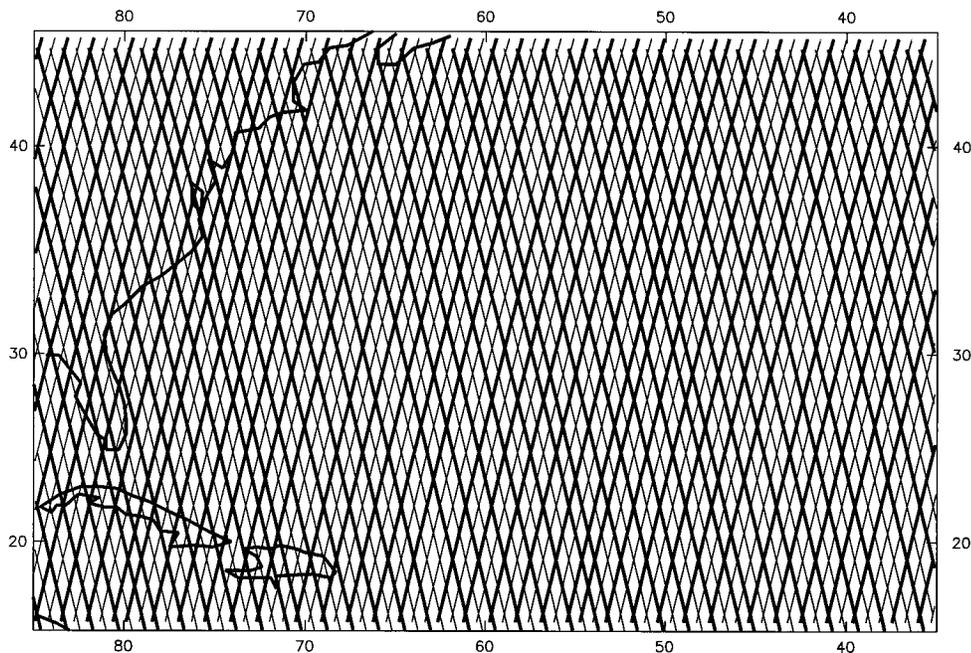
FIG. 6. The ground tracks for the ERS 35-day repeat period. Heavy lines are for days 0–17.5 and thin lines for days 17.5–35.

tracks that are much more coarsely spaced than those of either the Geosat or the ERS satellites. The dimensions of the interpolation grid of crossovers and diamond centers are $\Delta x \approx 1.4°$, $\Delta y \approx 2.8°$ (see Fig. 4b). The minimum spatial smoothing parameter required in order to satisfy the Nyquist sampling criterion for an interpolation grid consisting of crossovers and diamond centers is thus $d_s = 5.6°$.

The mean and variability of time series of RESB for smoothed estimates constructed at a TP diamond center and a crossover are contoured in Fig. 5c. Because of the coarse spacing of the TP ground tracks, the highest possible spatial resolution that satisfies the 10% RESB variability criterion is about 6.75°, which is achieved when $d_t \gtrsim 25$ days. These filter cutoffs are analogous to those obtained with $4° \times 15$ day block averages.

In addition to resolving shorter spatial scales (at the expense of somewhat greater temporal smoothing), the Geosat and ERS sampling patterns also yield improved overall accuracy at the coarse spatial scales resolvable by the TP sampling pattern. The relative accuracies of sea level fields constructed from the Geosat, ERS, and TP sampling patterns individually can be determined by comparing the left panels of Fig. 5. For the smoothing parameters (6°, 30 days), for example, the RESB magnitudes for Geosat, ERS, and TP are about 0.028, 0.026, and 0.076, respectively. The Geosat and ERS sampling patterns thus yield RESB values nearly three times smaller than that of the TP sampling pattern.

The conclusion that the Geosat and ERS sampling patterns yield smaller RESB than does the TP sampling pattern is at odds with the conclusion of Wunsch (1989).

As discussed in section 2, however, the two approaches address different questions. Wunsch's method determines the errors of sample estimates of individual Fourier harmonics. The method used here effectively determines the total errors over all Fourier harmonics. Our conclusion depends on the 50-km and 30-day decorrelation scales assumed here for the sea level variability (see appendix A). Wunsch's method is, of course, equally sensitive to the signal spectral characteristics, which were assumed to be uniformly distributed in frequency–wavenumber space by Wunsch (1989). It is unclear how incorporation of a more realistic signal spectrum would affect his conclusions about the relative merits of the TP and Geosat orbit configurations.

6. The mapping resolution capability of combined TP and ERS

The 2 October 1992–20 December 1993 and 21 March 1995–31 May 1996 overlaps of the 10-day repeat TP and 35-day repeat *ERS-1* altimeter missions and the currently simultaneous (since 29 August 1995) TP and 35-day repeat *ERS-2* altimeter missions offer the potential for higher spatial and temporal mapping resolutions by combining two datasets. The combined TP and ERS ground-track pattern is shown in Fig. 7a for a small portion of the North Atlantic. Although the geographical distribution of ERS ground tracks differs somewhat within each individual TP diamond because of the total lack of coordination of the two orbit configurations, this particular region is sufficiently representative for present purposes. The density of obser-
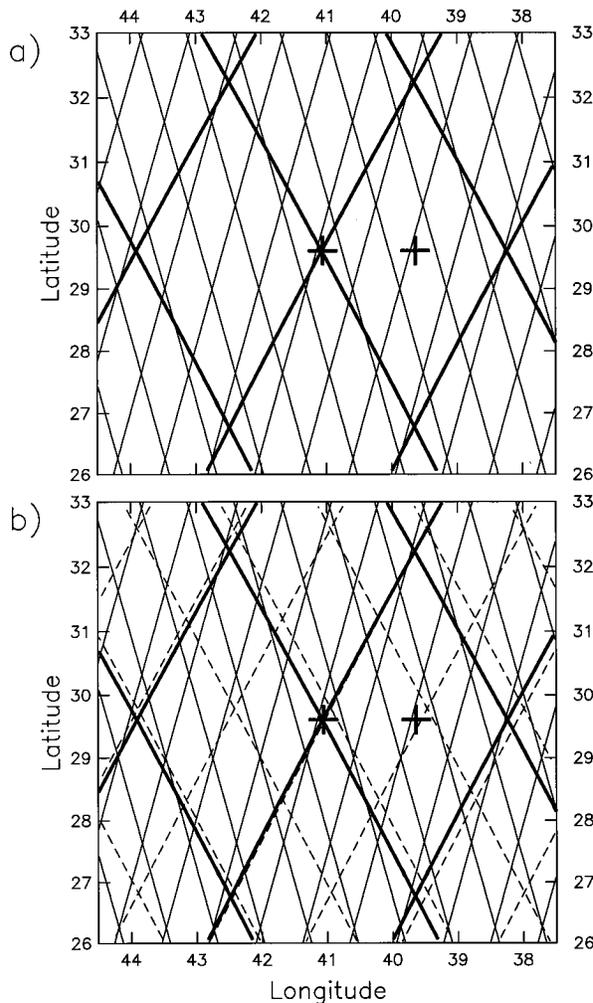
FIG. 7. The ground tracks for (a) the tandem TP–ERS mission and (b) the triplet TP–ERS–GFO mission. The heavy, thin, and dashed lines correspond to TP, ERS, and Geosat ground tracks, respectively. The crosses are the locations at which smoothed estimates are constructed for the RESB plots in Fig. 8.

vations near ERS crossover points varies considerably within the larger TP diamond region, depending on the proximity of the ERS crossover to the TP ground tracks.

Time series of the RESB were calculated for smoothed SSH estimates constructed at the TP diamond center and crossover shown in Fig. 7a from the combined ERS and TP sampling pattern. The period required for both satellites to return to their initial location is 70 days, which is the least common multiple of the 35-day ERS repeat and the 10-day TP repeat. It is therefore necessary to examine the RESB over a 70-day period.

The mean and variability of the RESB time series at the two locations for the combined TP–ERS altimeter missions are contoured in Fig. 8a. The results are quite surprising. The RESB variability plot for combined TP and ERS (right panel of Fig. 8a) is very similar to that for TP alone (right panel of Fig. 5c); a spatial resolution

of 6.75° can be achieved for temporal smoothing of d_t $\gtrsim$ 30 days. The RESB magnitude (left panel of Fig. 8a) at this resolution is about the same as that obtained from the Geosat or ERS sampling pattern alone (i.e., smaller by nearly a factor of 3 than that obtained from the TP sampling pattern alone) but is not sufficiently small to relax the 10% RESB variability criterion using the threshold value of 0.01 suggested in section 2b. We therefore conclude that the mapping resolution capability of the combined TP and ERS sampling pattern is no better than that of the TP sampling pattern alone. This is supported by the simulated examples in Fig. 2. The dense combined TP and ERS coverage in the vicinity of the TP ground tracks does not compensate for the comparatively sparse sampling from ERS alone in the centers of the diamond patterns mapped out by the TP ground tracks.

## 7. The mapping resolution capability of combined TP, *ERS-2*, and GFO

The planned launch of GFO in 1997 would provide the opportunity to obtain global observations of SSH from three simultaneous altimeters (TP, *ERS-2,* and GFO). The combined ground track for these three satellites is shown in Fig. 7b. As in the tandem TP–ERS mission considered in section 6, the sampling errors of this triplet altimeter mission are illustrated by considering the mean and variability of time series of RESB at a TP diamond center and crossover. It can be seen from the left panel of Fig. 8b that the overall mean RESB is reduced somewhat from the tandem TP–ERS mission. However, the RESB variability (right panel of Fig. 8b) is very similar to that of the tandem TP–ERS mission. The best combination of smoothing parameters is about $(d_s, d_t) = (6.75°, 35$ days), which is essentially the same as the tandem TP–ERS mission. The RESB for these smoothing parameters is reduced from 0.026 for the tandem mission to 0.020 for the triplet mission.

It is thus concluded that the addition of the GFO satellite does not significantly improve the mapping resolution capability beyond that which can be obtained from the combined TP and ERS sampling pattern or even from the TP sampling pattern alone. This is consistent with the simulated examples in Fig. 2.

8. The mapping resolution capability of combined TP and Jason

Planning is well under way for a joint United States–France TP follow-on altimeter mission called Jason, which has an expected launch date in December 1999. Although there is only a moderate probability of overlap between TP and Jason, it is useful to consider the mapping resolution capability of a coordinated tandem TP and Jason mission with the same 10-day repeat sampling period. Two potential tandem TP–Jason missions are investigated here.
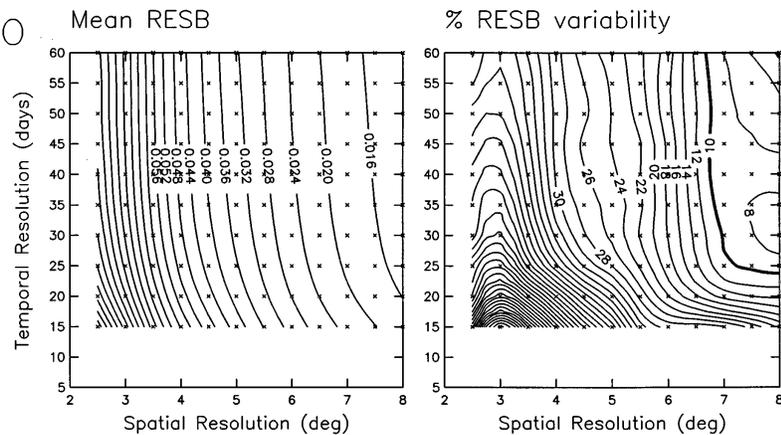
a) TP/ERS
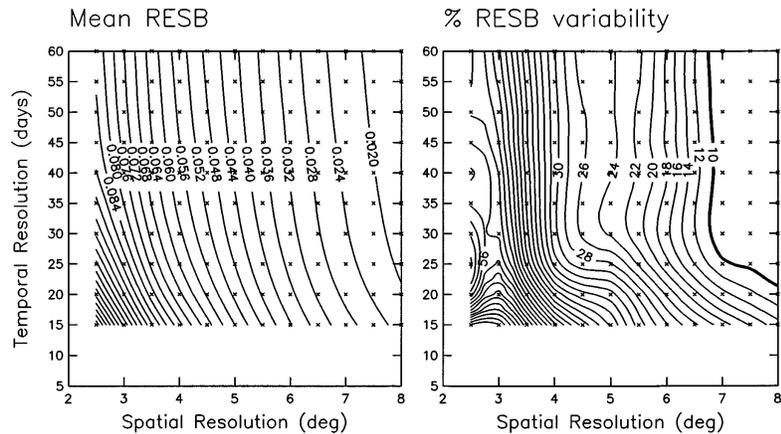
b) TP/ERS/GFO

FIG. 8. The same as Fig. 5 except for (a) the tandem TP–ERS mission and (b) the triplet TP–ERS–GFO mission. The RESB mean and variability were computed over a 70-day period at the locations shown in Fig. 7.

a. Scenario 1: 5-day offset along the same ground tracks

Present plans call for the Jason orbit ground tracks to be identical to those of TP in order to maintain a long record of SSH on a fixed sample grid. This choice is dictated by the interest in applications of altimeter data for studies of short-term climate variability of large-scale ocean circulation. The timing of Jason equatorial crossings has not yet been established. In the event of overlap between TP and Jason, the optimum lag between TP and Jason samples of the same ground track is probably 5 days. The diamond patterns mapped out by the combined TP and Jason ground tracks in this tandem orbit configuration would have the same midlatitude dimensions as TP alone.

The mean and variability of time series of RESB at a crossover and a diamond center are contoured in Fig. 9a. The mean RESB in the left panel of Fig. 9a is almost identical to that obtained from the TP sampling pattern alone (compare with the left panel of Fig. 5c). The addition of Jason does not significantly improve the overall accuracy of smoothed estimates of SSH because the spatial distribution of observations used to construct a

smoothed estimate is not improved when the TP and Jason ground tracks coincide. The 10% variability and Nyquist criteria are both satisfied for smoothed estimates constructed at crossovers and diamond centers when $(d_s, d_t) = (6.5°, 25$ days) for the 5-day offset tandem TP–Jason orbit scenario (right panel of Fig. 9a). This is the same temporal mapping resolution capability and a slightly improved spatial mapping resolution capability as can be obtained from the TP sampling pattern alone.

b. Scenario 2: 0-day offset along interleaved ground tracks

In the second tandem TP–Jason scenario considered here, the Jason orbit was chosen to be the present TP orbit and the TP orbit was adjusted to shift the ground tracks longitudinally so as to interleave the Jason ground tracks. If TP is still operational at the time of the Jason launch, it is anticipated that there will be sufficient fuel on board to adjust the TP orbit in this fashion. The timing of the two orbits was synchronized so that adjacent TP and Jason tracks were sampled simultaneous-

a) TP/Jason #1

Mean RESB

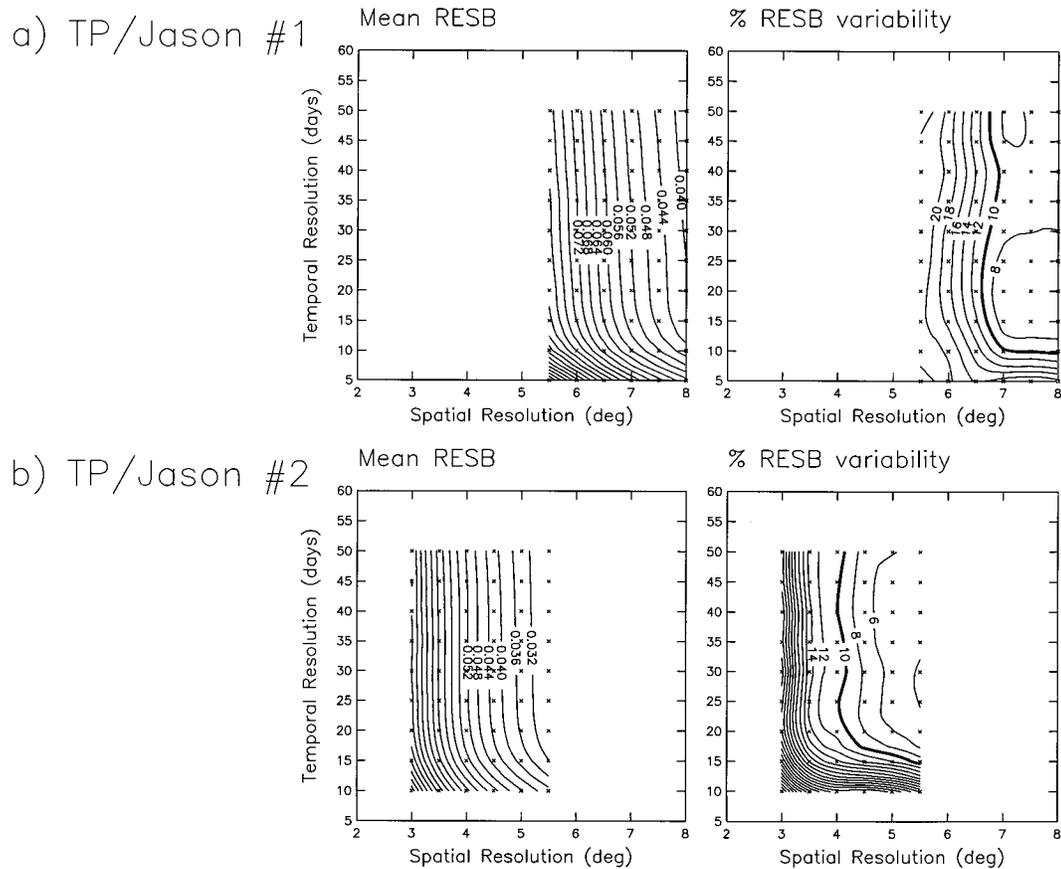% RESB variability

b) TP/Jason #2

Mean RESB

% RESB variability

FIG. 9. The same as Fig. 5 except for 10-day repeat tandem TP–Jason missions with (a) the 5-day offset, same ground-track scenario 1, and (b) the 0-day offset interleaved, ground-track scenario 2.

ly. The longitudinal and latitudinal separations of crossovers are therefore $\Delta\phi \approx 1.4°$ and $\Delta\theta \approx 2.8°$ at midlatitudes.

Time series of RESB were calculated at a crossover and a diamond center in the interleaved ground-track pattern. The mean and variability of these RESB time series are contoured in Fig. 9b. For smoothing parameters of $(d_s, d_t) = (5.5°, 25$ days$)$, for example, the increased spatial density of observations from the interleaved ground tracks reduces the magnitude of the RESB (left panel of Fig. 9b) by nearly a factor of 3 compared with that for TP alone or for the TP–Jason tandem orbit scenario 1 considered in section 7a. Moreover, the 10% RESB variability criterion is satisfied with a spatial resolution of about 4° when the temporal smoothing parameter is larger than about 25 days. This value of d_s also satisfies the Nyquist criterion for this sampling grid consisting of crossovers and diamond centers of the interleaved ground-track pattern of this tandem orbit configuration. This tandem orbit configuration thus offers a dramatic improvement of spatial mapping resolution capability.

9. The mapping resolution capability of combined *ERS-1* and *ERS-2*

The overlap of *ERS-1* and *ERS-2* from 29 August 1995 to 31 May 1996 offered a brief opportunity to construct high-resolution SSH fields from two altimeters simultaneously in orbit with the same 35-day repeat sampling period. Three possible *ERS-1–ERS-2* orbit scenarios are investigated in this section.

a. Scenario 1: 1-day offset

The first *ERS-1–ERS-2* orbit scenario considered here was the actual tandem orbit configuration for the overlap period 29 August 1995–31 May 1996, during which *ERS-2* sampled exactly the same ground tracks as *ERS-1* with a time lag of 1 day. This corresponds to a phase separation of approximately 120° in the same orbital plane. The ground tracks over a portion of the North Atlantic Ocean for a 3-day period of this tandem orbit scenario are shown in Fig. 10a. This pattern shifts westward in each successive 3-day period (see Fig. A2a in appendix A). As described in section 4, the two altim-
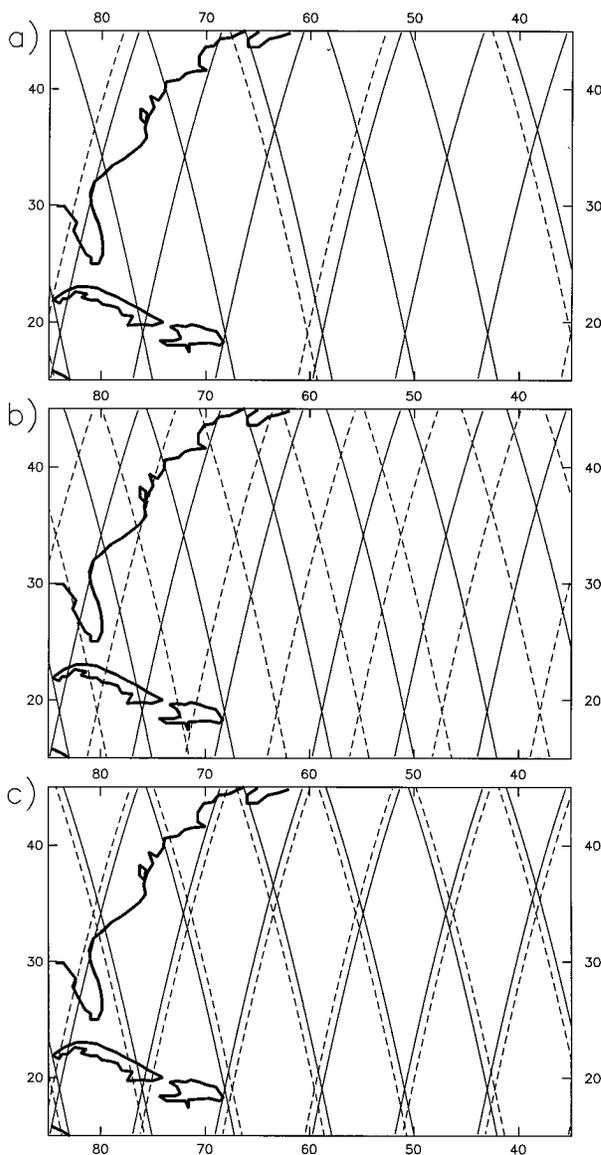
FIG. 10. The ground tracks over a portion of the North Atlantic Ocean for a 3-day period of tandem *ERS-1–ERS-2* missions with (a) the 1-day offset scenario 1, (b) the 8.75-day offset scenario 2, and (c) the 17.5-day offset scenario 3. In all cases, the solid lines are *ERS-1* and the dashed lines are *ERS-2*.

eters very nearly return to their initial locations after 17.5 days, except shifted longitudinally so as to interleave the ground tracks sampled during the first 17.5 days (see Fig. 6).

Only a few of the *ERS-2* ground tracks are visible in Fig. 10a because, with a 1-day offset between *ERS-1* and *ERS-2,* the two satellite ground tracks overlap during 2 days of each 3-day subcycle. With the 30-day SSH decorrelation timescale assumed here (appendix A), the *ERS-1* and *ERS-2* samples in this 1-day offset scenario are largely redundant for the smoothed SSH fields of interest here. Unless measurement errors are large, it

can be anticipated that the mapping resolution capability of the combined *ERS-1–ERS-2* sampling pattern for this tandem orbit configuration will be very similar to that of either ERS satellite alone (section 4).

This speculation is borne out in the RESB of smoothed estimates constructed at the same crossover and diamond center considered in section 4. The mean and variability of time series of RESB averaged over the two estimation locations and the 35-day repeat period (see Fig. 11a) are almost identical to those obtained for either ERS satellite alone (compare with Fig. 5b). The best mapping resolution is obtained with smoothing parameters $(d_s, d_t) = (3.5°, 50 \text{ days})$.
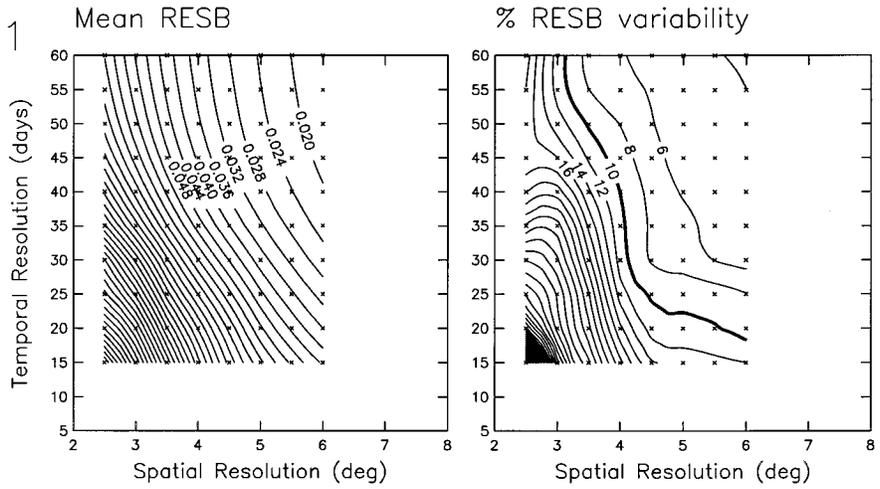
b. Scenario 2: 8.75-day offset

The second *ERS-1–ERS-2* tandem orbit scenario considered here consists of *ERS-2* samples lagged by 26.25 days relative to *ERS-1* samples along the same 35-day repeat ground track. This is equivalent to *ERS-2* leading *ERS-1* by 8.75 days. Early plans called for a shift of the orbital phase difference between *ERS-1* and *ERS-2* from the initial 120° to 180° at some time during the first year of the tandem mission. These plans were later abandoned when the decision was made to terminate the *ERS-1* altimeter mission on 31 May 1996. It is nonetheless useful to investigate the mapping resolution capability of this tandem orbit scenario. A 180° orbital phase difference results in a lag between *ERS-1* and *ERS-2* samples along the same ground track that is very close to the 8.75-day lag considered here.

The motivation for considering an 8.75-day offset tandem orbit scenario is the existence of the 17.5-day subcycle in the ERS 35-day repeat ground track pattern (Fig. 6). As previously noted, each ERS satellite samples essentially the same ground-track pattern every 17.5 days, except it is shifted longitudinally so that the ground tracks of the second half of the repeat cycle interleave those of the first half of the repeat cycle. Intuitively, this scenario seems a plausible candidate for an ''optimum'' tandem orbit configuration from the perspective of smoothed SSH fields constructed from the combined *ERS-1–ERS-2* sampling pattern.

The ground tracks over a portion of the North Atlantic Ocean for a 3-day period of this 8.75-day offset tandem orbit scenario are shown in Fig. 10b. As in Fig. A2a in appendix A, this pattern shifts westward in each successive 3-day period. The ground track pattern mapped out in 8.75 days by the two satellites in this scenario is essentially the same as that mapped out by either ERS satellite alone in a 17.5-day period.

The mean and variability of time series of RESB averaged over the two estimation locations and the 35-day repeat period are contoured in Fig. 11b. The magnitudes of the RESB are somewhat smaller in the lower half of the left panel of Fig. 11b than those shown in the left panel of Fig. 11a for the 1-day offset tandem orbit scenario. For larger values of d_t, however, the RESB is
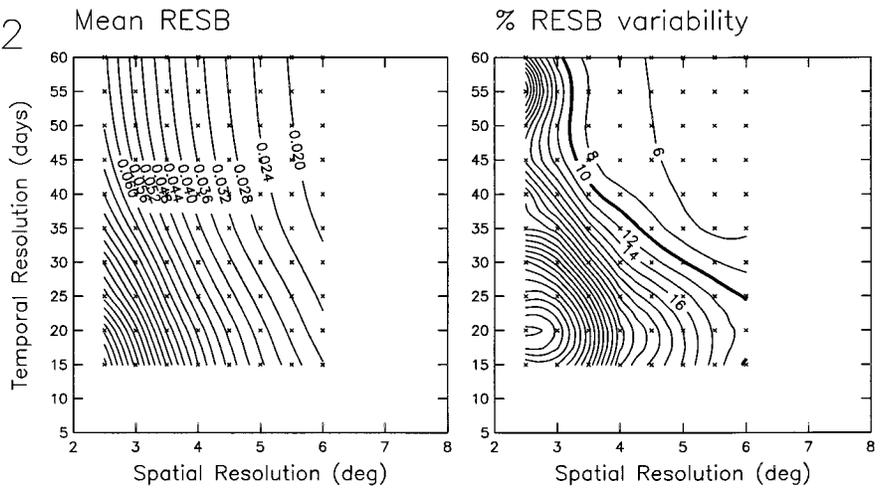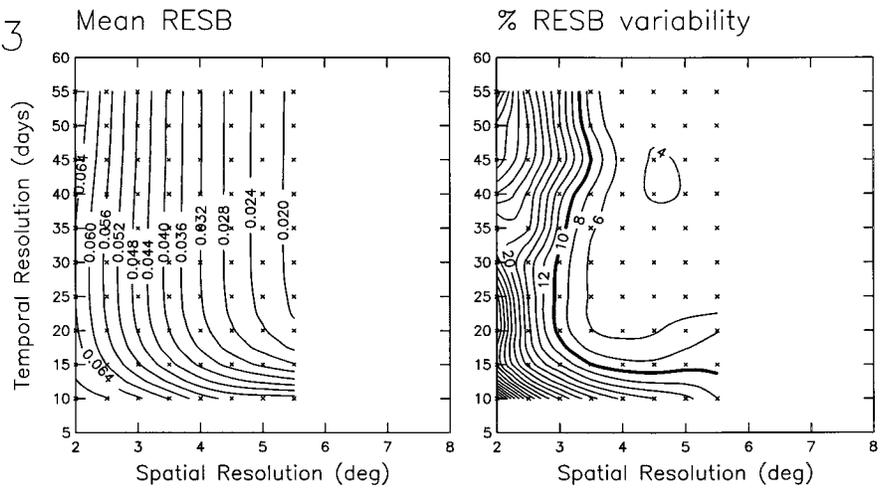
FIG. 11. The same as Fig. 5 except for 35-day repeat tandem *ERS-1–ERS-2* missions with (a) 1-day offset scenario 1, (b) 8.75-day offset scenario 2, and (c) 17.5-day offset scenario 3.

about the same for both orbit scenarios. Likewise, the RESB variability is larger for the 8.75-day offset scenario when d_t is small but is generally very similar to that for the 1-day offset scenario when d_t is large. There is a small improvement in spatial mapping resolution for d_t between about 45 and 60 days; the 10% RESB variability criterion is satisfied for $(d_s, d_t) = (3.25°, 45$ days). We conclude that this 8.75-day offset *ERS-1–ERS-2* tandem orbit scenario offers very little improvement over either ERS satellite alone or the 1-day offset tandem *ERS-1–ERS-2* orbit scenario considered in section 8a.

c. Scenario 3: 17.5-day offset

The third *ERS-1–ERS-2* tandem orbit scenario considered here consists of a 17.5-day offset in which *ERS-2* samples the same 35-day repeat ground track pattern as *ERS-1* at a 17.5-day lag. From the ground tracks mapped out during a 3-day period (Fig. 10c), this tandem orbit configuration results in parallel ground tracks separated longitudinally by approximately 0.7°. In this tandem orbit scenario, *ERS-1* samples one 17.5-day subcycle of the 35-day repeat period at the same time that *ERS-2* samples the other 17.5-day subcycle (see Fig. 6).

The resulting dense ground-track pattern greatly improves the spatial mapping resolution of smoothed SSH fields constructed from the combined *ERS-1* and *ERS-2* observations. The mean and variability of time series of RESB averaged over estimates constructed at crossovers and diamond centers are contoured in Fig. 11c. The magnitudes of the RESB are much smaller in the lower half of the left panel of Fig. 11c than those for the *ERS-1–ERS-2* tandem orbit scenarios considered in sections 8a and 8b. Moreover, the RESB variability is also much smaller for this tandem *ERS-1–ERS-2* orbit scenario. The 10% variability criterion is satisfied for $(d_s, d_t) = (3°, 20$ days). This represents a dramatic improvement in the temporal mapping resolution capability compared with the other tandem *ERS-1–ERS-2* missions considered here.

10. Discussion and conclusions

Examination of smoothed SSH maps constructed from simulated altimeter data (Figs. 1 and 2) graphically illustrates the spurious eddylike features that can arise from geographical variations of sampling errors in undersmoothed SSH fields. These undesirable features can be mitigated if the smoothing parameters and interpolation grid on which smoothed estimates are to be constructed are chosen appropriately. In this study, we have refined a method proposed by SC92 and CS94 for determining the spatial and temporal resolution capability of fields of a scalar variable constructed from an irregular sampling pattern. The method is based on smoothing the irregularly sampled data so that sampling errors are spatially and temporally homogeneous.

Sampling errors can be computed for an arbitrarily defined linear smoothing scheme based on a prescribed form for the wavenumber–frequency spectral characteristics of SSH. The spectral characteristics used here are derived from Gaussian autocorrelation functions with 50-km and 30-day decorrelation scales that have been shown from hydrographic and altimeter data to be appropriate at midlatitudes. The latitudinal variation of decorrelation length scales (longer at low latitudes and shorter at high latitudes) is offset to some extent by the latitudinal variation of the spatial separation of satellite ground tracks (more coarsely spaced at low latitudes and more densely spaced at high latitudes). Because of these partially compensating signal and sampling characteristics and the consideration of spatial smoothing in degrees rather than kilometers, the results presented here should be representative of a fairly broad range of latitudes.

Two criteria for determining the mapping resolution capability of an irregular sample pattern have been proposed. The first (which is the only criterion considered by CS94) is that the expected squared bias (ESB) of smoothed estimates must be spatially and temporally homogeneous. As defined in appendix A and section 2a, the ESB is the component of the total expected squared error of the estimates that is attributable to sampling errors. For convenience, the ESB is normalized by the signal variance to obtain the relative expected squared bias (RESB) so that sampling errors can be considered in relation to the typical magnitude of signal variations at the locations of interest. An operational definition of statistical homogeneity proposed here that we believe to be well suited to altimeter applications is that the RESB varies by less than 10% of its mean value averaged over all times and locations at which smoothed estimates are constructed.

The second criterion for determining the mapping resolution capability is that the Nyquist sampling theorem must be satisfied so that the wavenumbers and frequencies included in the smoothed estimates are resolvable by the chosen interpolation grid. In the case of the quadratic loess smoother used here (appendix B), this is equivalent to requiring that the smoothing parameters used to construct the smoothed estimates must be at least twice as large as the spatial and temporal dimensions of the interpolation grid. For the altimeter applications of interest here, we have considered estimation grids consisting of ground-track crossovers and diamond centers and estimation times consisting of daily intervals over the satellite repeat period.

It is important to recognize that there is no single combination of smoothing parameters that satisfies the two criteria outlined above. Spatial and temporal resolution can be traded off to obtain a continuum of smoothing parameters that satisfies the 10% RESB variability criterion. The "best" mapping resolution capability is defined here to be the highest spatial resolution that satisfies the 10% RESB variability criterion and the
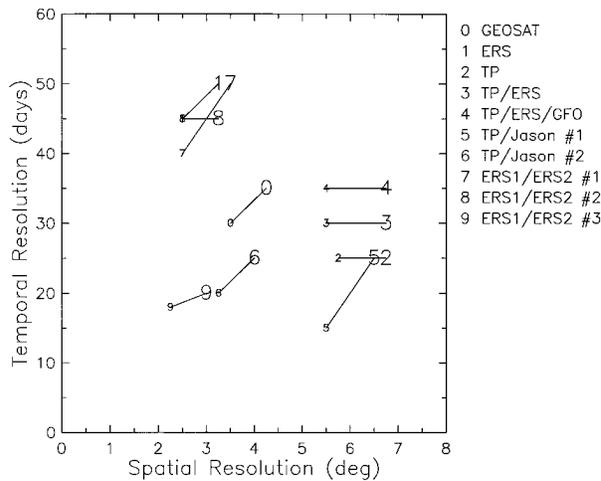
FIG. 12. A graphical summary of the "best" spatial and temporal mapping resolution capabilities of the single, tandem, and triplet altimeter missions considered in this study. As defined in section 2b, the best mapping resolution for the altimeter applications of interest here is the highest spatial resolution that satisfies both the RESB variability criterion and the Nyquist criterion of section 2a when the temporal resolution is less than or equal to 50 days. The large and small symbols in the figure correspond to the mapping resolution capabilities deduced with an RESB variability criterion of 10% and 20%, respectively. Legend at right defines the various altimeter datasets considered. The numbers on the tandem altimeter missions in the legend correspond to the tandem orbit scenarios considered in sections 8 and 9.

Nyquist criterion when the temporal resolution is 50 days or shorter. The choice of 50-day resolution is dictated by the interest in applications of altimeter data for investigating SSH variability on seasonal and longer timescales. A 50-day filter cutoff period corresponds very closely to the filtering characteristics of monthly means that are traditionally used to study low-frequency variability in the ocean. The quadratic loess smoother used here is far superior to the block average smoother because of the smaller sidelobes and sharper spectral rolloff of the filter transfer function near the low-pass cutoff frequency (see SC92).

The criteria outlined above were applied individually to the 17-day repeat Geosat, the 35-day repeat ERS, and the 10-day repeat TP altimeter sampling patterns. The resulting resolution capabilities of SSH fields constructed from altimeter data are summarized by the large symbols in Fig. 12. Not surprisingly, the spatial and temporal mapping resolutions of an individual mission are directly related to the repeat period and corresponding ground-track spacing of the orbit configuration. The temporal smoothing that yields the best possible spatial mapping resolution is roughly double the orbit repeat period; the best mapping resolution capabilities of the 17-day Geosat, 35-day ERS, and 10-day TP repeat orbits are obtained with temporal smoothing parameters of 35, 50, and 25 days, respectively. The corresponding spatial resolution capabilities of about 4.25°, 3.25°, and 6.75°

are somewhat less than three times the meridional spacing of crossovers at midlatitudes (see Fig. 4b). In some cases, the temporal smoothing can be decreased by as much as about a factor of 2 by increasing the spatial smoothing by about the same amount.

The mapping resolution capabilities deduced from the sophisticated method presented here do not differ greatly from the resolutions that would be crudely deduced from a simple consideration of the Nyquist sampling for synoptic grids of observations at the crossover points at time intervals equal to the orbit repeat period (a temporal resolution equal to twice the orbit repeat period and a spatial resolution equal to twice the meridional spacing of crossovers). For the purposes of constructing smoothed maps of SSH, the additional samples along the ground tracks between crossover points do not substantially improve the accuracies of the smoothed SSH fields in the error-free measurements considered here; the fundamental limitation is the large, unsampled diamond-shaped regions between ground tracks.

The existence of two separate altimeter satellites presently in orbit (TP and *ERS-2*) and the planned launch of GFO in 1997 offers the potential for greatly improved spatial and temporal mapping resolution of SSH variability by combining the data from more than one altimeter. As shown in Fig. 12, however, the degree to which the mapping resolution capability is improved depends strongly on the detailed characteristics of the combined sampling patterns; improved resolution can only be achieved through careful coordination of the satellite missions. This was demonstrated by consideration of the uncoordinated tandem TP–ERS mission and triplet TP–ERS–GFO mission, for both of which the resolution capability is not significantly improved over that obtained from the TP sampling pattern alone. Although the magnitudes of the mean RESB decrease when data from these multiple altimeters are combined, the spatial and temporal inhomogeneities are not significantly reduced from those obtained from TP data alone.

Consideration of various coordinated hypothetical tandem TP–Jason missions and actual and hypothetical tandem *ERS-1–ERS-2* missions showed that the highest mapping resolution is obtained from simultaneous interleaved ground tracks with the same orbit inclination and repeat period and no time offset between sampling of adjacent ground tracks of the two satellites. The reason that this offers the best mapping resolution capability is easily understood by considering the spatial and temporal scales assumed here for the mesoscale variability that is responsible for sampling errors in smoothed SSH fields constructed from altimeter data. The approximate 30-day timescales of mesoscale variability are relatively well resolved by the orbit repeat periods of any of the presently operational satellites (the 10-day TP orbit, the 17-day Geosat orbit, or the 17.5-day interleaved 35-day ERS orbit.) The short 50-km spatial scales of midlatitude mesoscale variability are comparatively poorly sampled by

the ground-track patterns of all of these satellites. For mapping midlatitude SSH variability on timescales longer than a few weeks, the spatial distribution of the altimeter observations thus imposes the most stringent constraint on the quality of the smoothed SSH estimates.

It was noted in section 2b that the RESB variability criterion can be relaxed if the magnitude of the RESB is sufficiently small. A somewhat arbitrary value of 0.01 (corresponding to a typical rms error of 1 cm) was suggested as a threshold RESB below which the variability criterion can be ignored. It was not possible to apply this threshold RESB criterion to any of the orbit configurations considered here; the RESB was never smaller than 0.01 when the RESB variability was 10%. For most of the sampling patterns considered here, relaxing the mean RESB threshold criterion to 0.04 (corresponding to a typical rms error of 2 cm) has no effect on the mapping resolution capabilities deduced here. The only exceptions are the tandem TP–ERS and triplet TP–ERS–GFO sampling patterns, for which the spatial mapping resolution capabilities improve from 6.75° to about 5.25° and 4.5°, respectively (see Fig. 8).

An important point to be emphasized is that an RESB variability criterion of 10% of the mean RESB can be considered illustrative of the technique proposed here. The mapping resolution capability can be deduced for any desired degree of RESB homogeneity based on the contour plots of RESB variability presented in sections 3–9. A more liberal specification of this criterion would render the above mapping resolution capabilities overly pessimistic. For example, the spatial mapping resolution capability typically improves by about 1° when the RESB variability criterion is relaxed to 20% (see small symbols in Fig. 12). The corresponding improvement in the temporal resolution ranges from 0 to 20 days, depending on the particular altimeter sampling pattern.

We close by noting that the results presented here have presumed complete sampling along the satellite ground tracks. In practice, data dropouts can occur in altimeter datasets as a result of errors in pointing angle, rain contamination, or numerous other factors. This creates even greater irregularity in the samples. Larger smoothing parameters may therefore be necessary to ensure that the filtering characteristics of the various orbit configurations are spatially and temporally homogeneous.

This analysis has also neglected the effects of measurement errors on the accuracies of SSH fields constructed from altimeter data. Le Traon and Nadal (1997, manuscript submitted to *J. Atmos. Oceanic Technol.*) have recently suggested that the effects of long-wavelength measurement errors may be significantly detrimental in smoothed maps of SSH. Depending on the magnitude and spectral characteristics of the measurement errors, this may necessitate even larger smoothing parameters than those deduced here based solely on sampling errors.

APPENDIX A

Technical Details of the Methodology

Consider a variable h that is a function of time t and two spatial dimensions x and y. In the present applications, h represents SSH variability. Any linear estimate $\hat{h}$ constructed at spatial and temporal location (x_0, y_0, t_0) from observations $g_j = h_j + \epsilon_j$ with measurement errors ϵ_j at N nearby locations (x_j, y_j, t_j) can be expressed in the general form

$$\hat{h}(x_0, y_0, t_0) = \sum_{j=1}^{N} \alpha_j(x_0, y_0, t_0)g_j, \quad \text{(A1)}$$

where α_j are the weights specified by the particular linear estimate that is used. In most applications, $\hat{h}(x_0, y_0, t_0)$ is an estimate of $h(x_0, y_0, t_0)$. More generally, however, $\hat{h}(x_0, y_0, t_0)$ can be any linear functional of the field $h(x, y, t)$. It is shown below that the spatial and temporal filtering properties of the linear estimate (A1) are prescribed by the specification of the weights α_j. The weights for a complicated linear smoother that is not naturally expressed in the form (A1) can be determined by the impulse response method (see, for example, appendix B).

The quality of the linear estimate (A1) is generally characterized by the expected squared error

$$\text{ESE}(x_0, y_0, t_0) = \langle [\hat{h}(x_0, y_0, t_0) - \bar{h}(x_0, y_0, t_0)]^2 \rangle, \quad \text{(A2)}$$

where the angle brackets are used to denote the expected value and $\bar{h}(x_0, y_0, t_0)$ is the true smoothed value for filter properties defined by the weights α_j. Given the autocovariance function of the signal of interest, an expression for the expected error of the estimate can be derived for any arbitrary linear objective estimate.

It is widely believed that the most useful linear estimate under all circumstances is the estimate obtained based on the Gauss–Markov theorem by minimizing the ESE. The α_j for this "optimal estimate" are computed from the space–time autocovariance functions of the signal $h(x, y, t)$ and measurement errors $\epsilon(x, y, t)$ (e.g., Gandin 1965; Alaka and Elvander 1972; Bretherton et al. 1976). [Optimal estimation is widely referred to for historical reasons by the misnomer "objective analysis"; all mathematically formulated estimates are, of course, objective. The term "linear objective estimate" is used here in the broader context to refer to any es-

timate of the form (A1).] In addition to minimizing the ESE, the advantage of optimal estimation is that the formalism allows an explicit treatment of measurement errors.

In practice, the optimal estimate is useful only when the spatial and temporal scales of $h(x, y, t)$ are adequately sampled by the observations. If the energetic scales of variability are undersampled (as they are, for example, in the altimeter observations of SSH variability that are of interest here), then the expected error of the optimal estimate can be highly inhomogeneous spatially and temporally. A common procedure for handling the problem of inhomogeneous errors of the optimal estimates is to artificially increase the spatial and/or temporal scales of the signal autocovariance function used to obtain the weights α_j. In addition to producing smoother estimates $\hat{h}(x, y, t)$, this procedure homogenizes the expected error field. It is important to note that, when the signal auto-covariance function is altered from its true value in this manner, the covariance-based objective estimates are no longer optimal and the error estimates are no longer quantitatively accurate (see examples in Chelton and Schlax 1991). The resulting estimates can be referred to as "Gauss–Markov estimates" to distinguish them from the optimal estimates.

The advantages of the Gauss–Markov covariance-based formulation over other forms of the objective estimate then become less clear when the covariance function is defined in an ad hoc manner. In fact, it may be disadvantageous to use the Gauss–Markov formulation since it is generally the most computationally intensive of all objective estimates.

The important point for present purposes is that the detailed formalism used to obtain the weights α_j is of secondary importance once it is accepted that some degree of smoothing must be applied to avoid practical difficulties associated with inhomogeneous estimation errors.

The filtering properties of the linear objective estimate have been discussed by SC92 and CS94, who showed that (A1) can be expressed in the wavenumber-frequency domain as

$$\hat{h}(x_0, y_0, t_0) = \int_{-\infty}^{\infty} \int_{-\infty}^{\infty} \int_{-\infty}^{\infty} \hat{P}^*(k, l, f; x_0, y_0, t_0)$$

$$\times\ G(k, l, f)\ dk\ dl\ df, \quad (A3)$$

where k, l are the zonal and meridional wavenumbers; f is the frequency; $G(k, l, f) = H(k, l, f) + E(k, l, f)$ is the sum of the Fourier transforms $H(k, l, f)$ and $E(k, l, f)$ of the signal $h(x, y, t)$ and measurement errors $\epsilon(x, y, t,)$ respectively; and

$$\hat{P}(k, l, f; x_0, y_0, t_0)$$

$$= \sum_{j=1}^{N} \alpha_j(x_0, y_0, t_0)\ \exp[-i2\pi(kx_j + ly_j - ft_j)] \quad (A4)$$

is the equivalent transfer function (ETF) developed by

SC92. It thus becomes apparent that the weights α_j in (A1) determine the filtering characteristics of the smoother. An efficient method for computing $\hat{P}$ by a fast Fourier transform technique is presented in the appendix of SC92.

The information content of the ETF for altimetric sampling of the sea level field has been illustrated by CS94 from a two-dimensional slice along the 90° azimuth (eastward) of the full three-dimensional ETF for a quadratic loess estimate constructed from the Geosat ground-track pattern. The analogous ETFs for the ERS and TP ground track patterns at 30°N are shown in Figs. A1a and A1b, respectively, for estimates constructed at a crossover point where ascending and descending ground tracks intersect.

At frequencies and wavenumbers where the ETF has a value of 1, all of the signal energy is included in the estimate. The signal is fully attenuated at frequencies and wavenumbers where the ETF is zero. The low-pass band of interest, where the magnitude of the ETF is close to 1, is evident at the center of the abscissa. Also apparent in the left half of Fig. A1a and the right half of Fig. A1b are ridges of "aliasing" peaks. As discussed by CS94, straight lines with slope ± 1 in log–log plots of the frequency–wavenumber ETF correspond to constant phase propagation with westward (slope of -1) or eastward (slope of $+1$) phase speed defined by the $\log f = 0$ intercept. The aliasing ridges in Fig. A1 represent propagation at approximately 50 km day^{-1} westward for ERS and 100 km day^{-1} eastward for TP. The significance of these aliasing ridges is that any propagating signal with spectral energy at these locations in frequency–wavenumber space will be aliased into the low-pass band.

Aliasing ridges occur in the ETF for every exact-repeat satellite orbit because of subcycles in the ground track repeat pattern. In the case of the ERS 35-day repeat orbit, they arise from the westward shift of a 3-day subcycle in the ERS ground track pattern. This can be seen in Fig. A2a, which shows the ground tracks for the first 9 days of the ERS 35-day repeat cycle over a portion of the North Atlantic Ocean. The westward shift that occurs every 3 days is approximately 150 km, thus accounting for the 50 km day^{-1} aliasing ridge in the ETF. The sampling characteristics of the ERS ground track pattern are discussed in further detail in section 4. A similar 3-day subcycle, which is eastward by approximately 300 km every 3 days (i.e., 100 km day^{-1}), is evident in the TP 10-day repeat cycle (Fig. A2b). The 3-day subcycle in the Geosat 17-day repeat cycle shifts eastward by approximately 50 km day^{-1} (see Fig. 5 of CS94).

As noted above, the quality of the objectively smoothed estimates (A1) can be assessed from the expected squared error (A2), which can be expanded as

$$\langle[\hat{h} - \bar{h}]^2\rangle = \langle[\hat{h} - \langle\hat{h}\rangle]^2\rangle + \langle[\bar{h} - \langle\hat{h}\rangle]^2\rangle. \quad (A5)$$

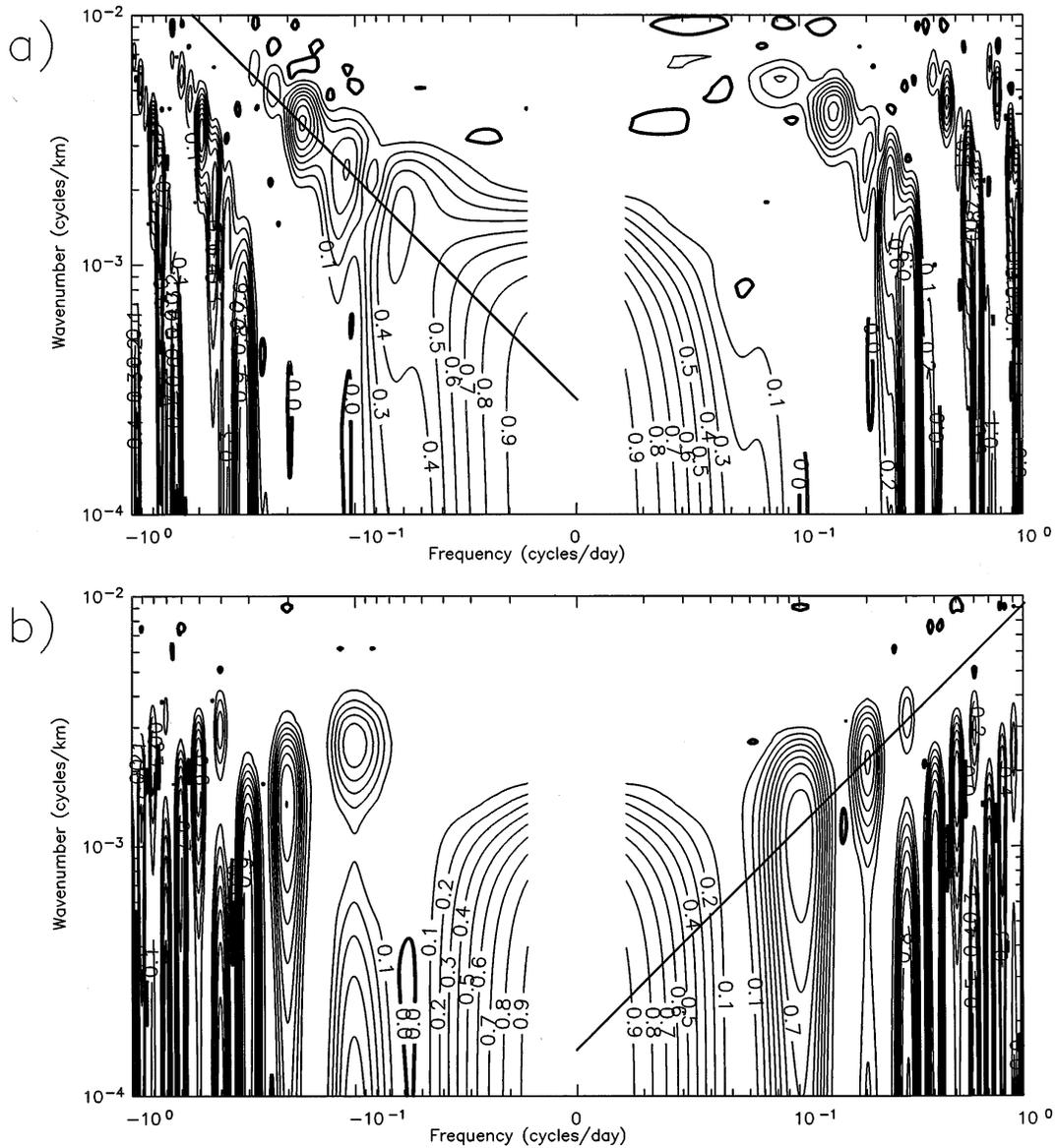The first term on the right side of (A5) is the variance

FIG. A1. A slice along the 90° azimuth (eastward) through the three-dimensional equivalent transfer function (ETF) for (a) the ERS and (b) the TP sampling patterns at 30°N for smoothed estimates constructed at crossover locations with isotropic spatial half-spans of $d_s = 8°$ and temporal half-spans of $d_t = 35$ days. The straight lines in each figure delineate the aliasing ridges discussed in the text.

(VAR) of the estimate $\hat{h}$ and the second term is the expected squared bias (ESB) of the estimate. These two contributions to the expected squared error can be expressed in the frequency domain as

$$\text{VAR}(x_0, y_0, t_0)$$

$$= \langle [\hat{h} - \langle \hat{h} \rangle]^2 \rangle$$

$$= \int_{-\infty}^{\infty} \int_{-\infty}^{\infty} \int_{-\infty}^{\infty} |\Delta \hat{P}|^2 S_\epsilon(k, l, f) \, dk \, dl \, df, \quad \text{(A6)}$$

$$\text{ESB}(x_0, y_0, t_0)$$

$$= \langle [\bar{h} - \langle \hat{h} \rangle]^2 \rangle$$

$$= \int_{-\infty}^{\infty} \int_{-\infty}^{\infty} \int_{-\infty}^{\infty} |\Delta \hat{P}|^2 S_h(k, l, f) \, dk \, dl \, df, \quad \text{(A7)}$$

where $S_\epsilon(k, l, f)$ is the wavenumber–frequency power spectral density of the measurment errors ϵ_j, $S_h(k, l, f)$ is the power spectral density of the signal $h(x, y, t)$, and $\Delta \hat{P} \equiv \hat{P} - P$ represents the imperfections of the ETF (A4) compared with the transfer function P of the ideal
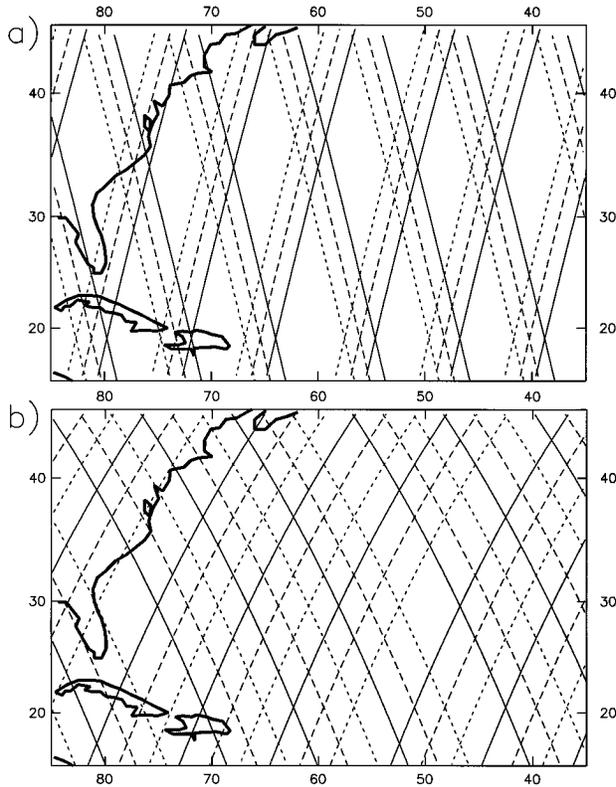
FIG. A2. The ground tracks over a portion of the North Atlantic Ocean for the first 9 days of (a) the 35-day ERS repeat period, and (b) the 10-day TP repeat period. In both cases, the solid, dashed, and dotted lines correspond, respectively, to days 1–3, days 4–6, and days 7–9 of the satellite orbital repeat period. There is a 3-day subcycle in both orbit configurations that shifts 150 km westward every 3 days in (a) and 300 km eastward every 3 days in (b).

low-pass filter. The ideal filter passes 100% of the signal at frequencies and wavenumbers below the cutoff frequency f_c and cutoff wavenumbers k_c and l_c and none of the signal at higher frequencies and wavenumbers. This is shown in SC92 and CS94 to be

$$P(k, l, f; x_0, y_0, t_0, k_c, l_c, f_c)$$

$$= \begin{cases} \exp[-i2\pi(kx_0 + ly_0 - ft_0)], \\ \quad \left(\frac{k}{k_c}\right)^2 + \left(\frac{l}{l_c}\right)^2 + \left(\frac{f}{f_c}\right)^2 < 1 \quad \text{(A8)} \\ 0, \quad \text{otherwise.} \end{cases}$$

The errors of the smoothed fields owing to measurement errors are thus described completely by the variance (A6). For the altimetric application of interest here, the total uncertainty of smoothed SSH fields is generally dominated by the sampling error component (Wunsch 1989), which is wholly embodied in the ESB (A7). Since this study is interested in the effects of sampling errors from the different orbit configurations, irrespective of any altimeter measurement errors, we will consider only the ESB as a measure of the accuracy of the smoothed

estimates. The smoothing parameters required to meet the mapping resolution capability criteria set forth in section 2 are therefore probably overly optimistic.

An important point to be emphasized is that the ESB depends only on the estimation location (x_0, y_0, t_0) and on the observation locations (x_j, y_j, t_j) [in order to determine the weights α_j in the linear estimate (A1) and hence the ETF (A4)] and on the power spectral density S_h of signal of interest. Actual data values are therefore not required in order to estimate the ESB. For the SSH applications of interest here, S_h was derived from the Fourier transform of a signal autocorrelation function that is Gaussian in both space and time with an isotropic spatial decorrelation scale of 50 km and a temporal decorrelation scale of 30 days. This correlation function was deduced from midlatitude hydrographic data by Shen et al. (1986) and is consistent with midlatitude altimetric estimates by Stammer (1997, manuscript submitted to *J. Phys. Oceanogr.*).

APPENDIX B

Quadratic Loess Smoothers

Loess smoothers are discussed extensively by Cleveland and Devlin (1988) and SC92. A brief summary of the mathematical details is given here. The one-dimensional quadratic loess estimate at time t_0 is defined to be a local weighted least squares fit of a quadratic function of t to N observations near t_0,

$$\hat{h}(t) = a_1 + a_2 t + a_3 t^2. \quad \text{(B1)}$$

The smoothed estimate is the least squares fit (B1) evaluated at t_0. The coefficients a_1, a_2, and a_3 are determined by minimizing the function

$$\Phi = \frac{1}{W} \sum_{j=1}^{N} w_j^2 (\hat{h} - h)^2, \quad \text{(B2)}$$

where W is the sum of the weights w_j, which are defined by the bell-shaped function

$$w_j = \begin{cases} (1 - q_j^3)^3, & 0 \le q_j \le 1 \\ 0 & q_j > 1 \end{cases} \quad \text{(B3a)}$$

$$q_j = \left(\frac{t_j - t_0}{d_t}\right)^2. \quad \text{(B3b)}$$

The parameter d_t is the half-span of the loess smoother.

The loess smoother formalism is easily extended to three dimensions, in which case there are 10 least squares parameters a_i and the bell-shaped weighting function (B3b) becomes ellipsoidal with half-spans d_x, d_y, and d_t,

$$q_j = \left[\left(\frac{x_j - x_0}{d_x}\right)^2 + \left(\frac{y_j - y_0}{d_y}\right)^2 + \left(\frac{t_j - t_0}{d_t}\right)^2\right]. \quad \text{(B4)}$$

The quadratic loess estimate can be expressed in the standard form (A1) of a linear estimate by the impulse

response method. This is most easily seen when the linear estimate (A1) is expressed as integrals over x, y, and t,

$$\hat{h}(x_0, y_0, t_0) = \int_{-\infty}^{\infty} \int_{-\infty}^{\infty} \int_{-\infty}^{\infty} \hat{p}(x, y, t; x_0, y_0, t_0)$$
$$\times g(x, y, t)\, dx\, dy\, dt, \quad (B5)$$

where $g(x, y, t)$ is the observed value of $h(x, y, t)$, including any measurement errors $\epsilon(x, y, t)$ and

$$\hat{p}(x, y, t; x_0, y_0, t_0)$$
$$= \sum_{j=1}^{N} \alpha_j(x_0, y_0, t_0)\delta(x - x_j)\delta(y - y_j)\delta(t - t_j). \quad (B6)$$

Suppose that the only observation is $g_k = 1$. In this case, $g(t)$ is an impulse at (x_k, y_k, t_k). By the sifting property of the Dirac delta functions (Bracewell 1986), the loess smoothed estimate then reduces to

$$\hat{h}(x_0, y_0, t_0)$$
$$= \hat{p}(x_k, y_k, t_k; x_0, y_0, t_0)$$
$$= \sum_{j=1}^{N} \alpha_j(x_0, y_0, t_0)\delta(x_k - x_j)\delta(y_k - y_j)\delta(t_k - t_j)$$
$$= \alpha_k(x_0, y_0, t_0). \quad (B7)$$

The smoother weight for the observation at (x_k, y_k, t_k) is therefore the quadratic loess smoothed estimate (B7) obtained by replacing the N observations with a single observation that has unit value at (x_k, y_k, t_k) and values of zero at all other observation points. The N smoother weights α_j in (A1) are thus derived by constructing N such quadratic loess estimates, one for an impulse function at each observation point (x_j, y_j, t_j).

After obtaining the weights α_j for the particular smoothing parameters d_x, d_y, and d_t by the impulse response method, it is straightforward to determine the filtering characteristics of the quadratic loess smoother from the ETF defined in appendix A. The ETFs for one-dimensional quadratic loess smoothers with evenly and irregularly spaced observations have been shown in Fig. 2 of CS94. The filtering properties of the loess smoother are defined by the half spans d_x, d_y, and d_t. The low-pass "cutoff frequency" for a temporal half span of d_t is approximately d_t^{-1} (see Fig. 2 of CS94). Similarly, the low-pass "cutoff wavenumber" for a spatial half-span of d_s is approximately d_s^{-1}. An important point to be noted is that the filtering properties of the loess smoother depend only on the spans d_x, d_y, and d_t and not the space–time autocovariance function of the signal of interest.

To place the filtering properties of the loess smoother in a more familiar context, the half amplitude cutoff frequency of the loess smoother with half-span d_t is approximately the same as that of a simple block average of width $0.6d_t$ (Chelton et al. 1990; SC92). A loess smoothed estimate with a half-span of 50 days, for example, is thus analogous to a 30-day block average. The filter transfer function of the loess smoother is far better, however, with a steeper filter rolloff near the cutoff frequency and smaller high-frequency filter sidelobes than the block average.

REFERENCES

Alaka, M. A., and R. C. Elvander, 1972: Optimum interpolation from observations of mixed quality. *Mon. Wea. Rev.,* **100,** 612–624.

Bracewell, R. N., 1986: *The Fourier Transform and its Applications.* McGraw-Hill, 474 pp.

Bretherton, F. P., R. E. Davis, and C. B. Fandry, 1976: A technique for objective analysis and design of oceanographic experiments applied to MODE-73. *Deep-Sea Res.,* **23,** 559–582.

Chelton, D. B., and M. G. Schlax, 1991: Estimation of time averages from irregularly spaced observations: With application to Coastal Zone Color Scanner estimates of chlorophyll concentration. *J. Geophys. Res.,* **96,** 14 669–14 692.

——, and ——, 1994: The resolution capability of an irregularly sampled dataset: With application to Geosat altimeter data. *J. Atmos. Oceanic Technol.,* **11,** 534–550.

——, ——, D. L. Witter, and J. G. Richman, 1990: Geosat altimeter observations of the surface circulation of the Southern Ocean. *J. Geophys. Res.,* **95,** 17 877–17 903.

Cleveland, W. S., and S. J. Devlin, 1988: Locally weighted regression: An approach to regression analysis by local fitting. *J. Amer. Stat. Assoc.,* **83,** 596–610.

Dukowicz, J. K., and R. D. Smith, 1994: Implicit free-surface method for the Bryan–Cox–Semtner ocean model. *J. Geophys Res.,* **99,** 7991–8014.

Gandin, L. S., 1965: *Objective Analysis of Meteorological Fields.* Israel Program for Scientific Translations, 242 pp.

McClean, J. L., A. J. Semtner, and V. L. Zlotnicki, 1996: Comparisons of mesoscale variability in the Semtner–Chervin quarter-degree model, the Los Alamos POP sixth-degree model, and TOPEX/ POSEIDON data. *J. Geophys. Res.,* in press.

Schlax, M. G., and D. B. Chelton, 1992: Frequency domain diagnostics for linear smoothers. *J. Amer. Stat. Assoc.,* **87,** 1070–1081.

Shen, C. Y., J. C. McWilliams, B. A. Taft, C. C. Ebbesmeyer, and E. J. Lindstrom, 1986: The mesoscale spatial structure and evolution of dynamical and scalar properties observed in the northwestern Atlantic Ocean during the POLYMODE Local Dynamics Experiment. *J. Phys. Oceanogr.,* **16,** 454–482.

Stammer, D., R. Tokmakian, A. Semtner, and C. Wunsch, 1996: How well does a 1/4° global circulation model simulate large-scale oceanic observations? *J. Geophys. Res.,* **101,** 25 799–25 811.

Treguier, A. M., 1992: Kinetic energy analysis of an eddy resolving, primitive equation model of the North Atlantic. *J. Geophys. Res.,* **97,** 687–701.

Verron, J., L. Cloutier, and P. Gaspar, 1996: Assessing dual-satellite altimetric missions for observing the midlatitude oceans. *J. Atmos. Oceanic Technol.,* **13,** 1073–1089.

Wilkin, J. L., and R. A. Morrow, 1994: Eddy kinetic energy and momentum flux in the Southern Ocean: Comparison of a global eddy-resolving model with altimeter, drifter, and current-meter data. *J. Geophys. Res.,* **99,** 7903–7916.

Wunsch, C., 1989: Sampling characteristics of satellite orbits. *J. Atmos. Oceanic Technol.,* **6,** 891–907.